Molecular Cell

Article

NAC promotes co-translational protein folding at the ribosomal tunnel exit

Graphical abstract

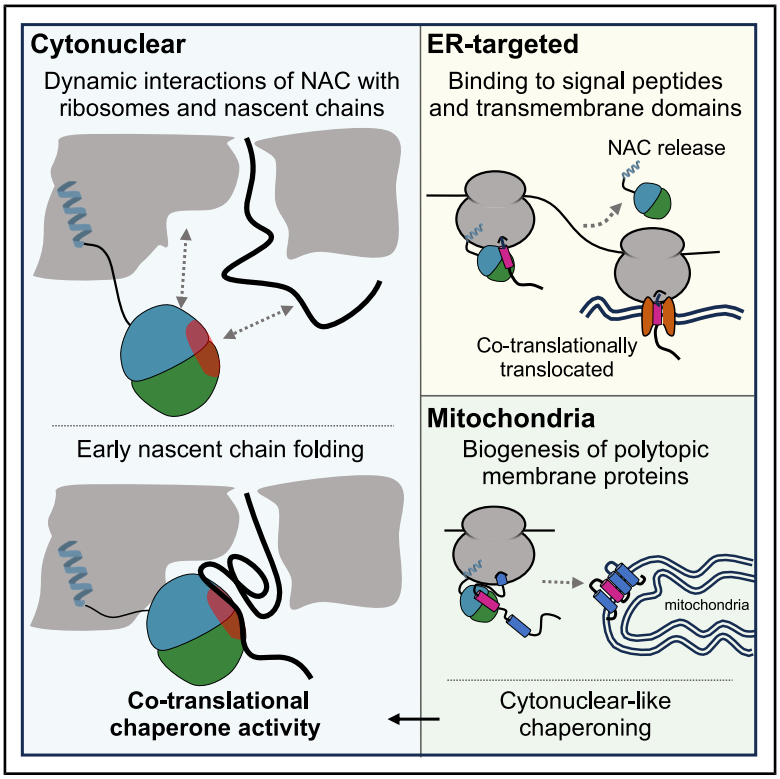

Highlights

- Selective ribosome profiling maps NAC's co-translational nascent chain interactome
- The NAC β-barrel domain dynamically engages nascent chains and the ribosome surface
- NAC assists early folding steps of cytonuclear protein domains at the tunnel exit
- NAC uses a tunnel-exit-oriented hydrophobic patch to bind and fold nascent chains

Authors

Jaime Santos, Manuel Günnigmann, Radoslaw J. Gora, ..., Shu-ou Shan, Günter Kramer, Bernd Bukau

Correspondence

ban@mol.biol.ethz.ch (N.B.), s.tans@amolf.nl (S.J.T.), sshan@caltech.edu (S.-o.S.), g.kramer@zmbh.uni-heidelberg.de (G.K.), bukau@zmbh.uni-heidelberg.de (B.B.)

In brief

Santos et al. reveal NAC's co-translational interactome, showing compartment-specific nascent chain interactions in human cells. NAC engages emerging chains at the ribosomal tunnel exit via a ribosome-oriented hydrophobic pocket, promoting early domain folding without stabilizing intermediate structures. These findings establish NAC as a co-translational chaperone integrating folding with protein biogenesis.

Santos et al., 2026, Molecular Cell *86*, 1311–1326
April 2, 2026
https://doi.org/10.1016/j.molcel.2026.02.022

CellPress

Molecular Cell

CellPress
OPEN ACCESS

Article

NAC promotes co-translational protein folding at the ribosomal tunnel exit

Jaime Santos,[1,6] Manuel Günnigmann,[1,6] Radoslaw J. Gora,[2,6] Marija Iljina,[3,4] Masa Predin,[5] Ilgin Eser Kotan,[1] Pratiman De,[2] Dhawal Choudhary,[3,4] Juwon Jang,[5] Frank Tippmann,[1] Christopher Hins,[3,4] Nenad Ban,[5,*] Sander J. Tans,[3,4,*] Shu-ou Shan,[2,*] Günter Kramer,[1,*] and Bernd Bukau[1,7,*]

[1]Center for Molecular Biology of the University of Heidelberg (ZMBH), DKFZ-ZMBH Alliance, Heidelberg, Germany
[2]Division of Chemistry and Chemical Engineering, California Institute of Technology, Pasadena, CA, USA
[3]Autonomous Matter Department, AMOLF, Science Park 104, 1098 Amsterdam, the Netherlands
[4]Bionanoscience Department, Kavli Institute of Nanoscience Delft, Delft University of Technology, Delft, the Netherlands
[5]Department of Biology, Institute of Molecular Biology and Biophysics, ETH Zurich, 8093 Zurich, Switzerland
[6]These authors contributed equally
[7]Lead contact
*Correspondence: ban@mol.biol.ethz.ch (N.B.), s.tans@amolf.nl (S.J.T.), sshan@caltech.edu (S.-o.S.), g.kramer@zmbh.uni-heidelberg.de (G.K.), bukau@zmbh.uni-heidelberg.de (B.B.)
https://doi.org/10.1016/j.molcel.2026.02.022

SUMMARY

The nascent polypeptide-associated complex (NAC) coordinates enzymatic modifications and membrane targeting of nascent chains during translation. While the role of NAC as a dynamic hub for other factors is well established, its direct role in co-translational folding is unclear. By proteome-wide profiling of co-translational NAC interactions in human cells, we found that NAC recognizes emerging segments enriched in hydrophobicity and α-helical propensity within folded domains of cytonuclear proteins. Single-molecule and structural analyses reveal that NAC, via its β-barrel domain, dynamically interacts with nascent chains at the ribosomal tunnel exit and is capable of promoting on-pathway folding. Compartment-specific nascent chain interactions of NAC further elucidate its role in targeting to the endoplasmic reticulum and in mitochondrial membrane protein biogenesis. Together, these findings show that human NAC acts as a bona fide co-translational chaperone that directly promotes early protein folding at the ribosomal tunnel exit, expanding its functional repertoire in protein biogenesis.

INTRODUCTION

To achieve biological activity, newly synthesized proteins must adopt their native structures, undergo N-terminal processing, and be targeted to specific cellular compartments. These processes begin co-translationally, mediated by numerous factors that interact with the growing polypeptide chains.[1–10] The nascent polypeptide-associated complex (NAC) is unique among these factors. By binding near the ribosomal polypeptide exit tunnel,[3,11,12] NAC serves as a coordinating hub, recruiting other factors to the ribosome and regulating their access to nascent chains.[2–4,13–15] Hence, NAC is implicated in various co-translational processes, including nascent chain targeting to the endoplasmic reticulum (ER) and mitochondria and coordination of enzymatic modifications.[2–4,12,13,16]

NAC is a highly conserved heterodimeric complex comprising NACα and NACβ (also known as BTF3 in humans). Its binding to the ribosome is primarily mediated by a positively charged anchor motif in the N terminus of NACβ (Figure 1A).[17,18] The central β-barrel domain, formed by both subunits (Figure 1A), interacts with the ribosome near the polypeptide tunnel exit. This interaction is dynamic and can be displaced, allowing nascent chains to become accessible to other biogenesis factors.[3,4] The C-terminal tails of NACα and NACβ help recruit various factors, including the signal recognition particle (SRP), methionine amino peptidase (MetAP1), N-acetyl transferase A (NatA), and the eEF1A-specific chaperone Chp1 (Figure 1A),[3,4,13,14] establishing NAC's role as a hub for nascent chain-interacting factors.

In addition to its coordinating roles, NAC has been proposed to function as a chaperone,[21–25] though its exact role in nascent chain folding is unclear. NAC inhibits protein aggregation post-translationally,[26–28] but evidence for a chaperoning function at the ribosome is indirect. NAC depletion in human and yeast increases the ubiquitination of nascent chains,[22,23] and simultaneous deletion of NAC and the Hsp70 homolog Ssb in yeast elevates protein aggregation.[29] Since NAC acts as a central coordinator of co-translational factors,[2–4,14] phenotypes initially linked to its proposed chaperone role may arise indirectly from the missing regulatory activity. Thus, the co-translational folding function of NAC remains a topic of debate.

Here, we characterize NAC interactions with nascent chains at a proteome-wide scale *in vivo* and investigate its chaperoning

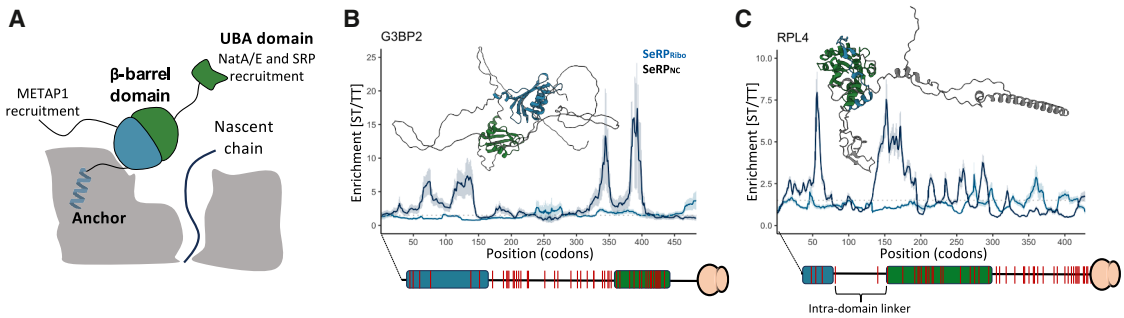

Figure 1. Structural features of NAC and development of a selective ribosome profiling strategy

(A) Schematic of NAC association with the ribosome and domain architecture of NACα (green) and NACβ (blue).

(B and C) Enrichment profiles of nascent cytonuclear proteins Ras GTPase-activating protein-binding protein 2 (G3BP2) and ribosomal protein L4 (RPL4). The nascent chain-independent ($SeRP_{ribo}$, blue) and -dependent ($SeRP_{NC}$, black) enrichments are shown. The protein domains (rectangles) and lysines (red bars) are annotated using a 30-residue tunnel correction, as depicted in Figure S1A. The structures were extracted from AlphaFold.[19,20] The dotted line indicates the enrichment threshold (1.5) used to define binding periods. The shaded areas indicate 95% confidence intervals.

functions *in vitro*. By developing NAC-selective ribosome profiling (SeRP) and integrating it with single-molecule Förster resonance energy transfer (smFRET), single-particle cryo-electron microscopy (cryo-EM), and optical tweezer experiments, we describe the basis of NAC's co-translational chaperoning activities. We show that NAC's β-barrel domain engages emerging polypeptides at the ribosomal tunnel exit, promoting early folding events. NAC chaperoning facilitates on-pathway folding of a model protein while preventing incomplete folding intermediates. Our SeRP analysis further reveals compartment-specific nascent chain binding functions, consistent with NAC's role in targeting ER-translocated proteins, chaperoning cytonuclear and mitochondrial proteins, and assisting mitochondrial membrane protein biogenesis. Collectively, these findings provide a comprehensive view of NAC-mediated protein biogenesis and define the chaperoning activity of this central ribosome-associated factor.

RESULTS

Design of a NAC-SeRP strategy

To investigate NAC's role in protein biogenesis, we developed a SeRP strategy to analyze its interactions with the nascent proteome of human HEK293-T cells. SeRP enables the mapping of nascent chain interactions during active translation in the cell, allowing the systematic analysis of co-translational processes with a codon resolution, such as chaperone engagement and complex assembly.[8,10,30–36] This approach builds on the ribosome profiling method,[37] where deep sequencing of ~30-nt nuclease-protected mRNA fragments reveals ribosome positions across the transcriptome with codon-level accuracy. In SeRP, this concept is extended by comparing the total translatome (TT), representing all translating ribosomes, with the selected translatome (ST), comprising ribosomes immunopurified through their association with the factor of interest.[33,36] The differential enrichment of ST/TT along coding sequences reveals when a factor engages ribosome-nascent chain complexes (RNCs) across the proteome (Figure S1A).

NAC binds to all translating ribosomes with a low nanomolar dissociation constant (K_d ~1 nM) via its anchor motif (Figure 1A) regardless of nascent chain nature.[3,17,18,38,39] The outlined SeRP method (termed $SeRP_{ribo}$) will therefore capture nascent chain-independent interactions, providing a comprehensive view of NAC's ribosome association.

To understand NAC binding to nascent chains, we employed an alternative strategy. In SeRP, crosslinking approaches are often employed to stabilize chaperone-RNC complexes.[32,36,40] Using the lysine-specific homo-bifunctional crosslinker DSP (dithiobis(succinimidylpropionate)), we found that NAC preferentially crosslinks to nascent chains of varying lengths instead of ribosomal proteins, as indicated by a smear rather than discrete bands in non-reducing western blots (Figure S1B). Notably, the lysines in the ribosome docking site of NAC contact ribosomal RNA instead of protein and are therefore not expected to generate NAC-ribosome crosslinks[3] (Figure S1C). To enrich crosslinked NAC-nascent chain complexes, we took advantage of the fact that NAC dissociates from ribosomes during sucrose cushion and gradient fractionation (Figures S1D and S1E). *In vivo* crosslinking prior to this fractionation yielded a 3-fold increase in NAC co-sedimentation with ribosomes, indicating stabilized NAC-nascent chain complexes (Figure S1E). DSP does not react with RNA and therefore does not interfere with footprint generation,[36] and its role is restricted to selectively reinforcing NAC-RNC interactions during purification. Overall, by generating a fraction enriched for these specific nascent chain interactions, this approach (termed $SeRP_{NC}$) enables the selective capture of NAC interactions with nascent chains.

We tested both SeRP strategies in HEK293-T cells (Figure S1F) and initially analyzed five cytonuclear proteins as a reference (Figures 1B, 1C, and S1G–S1I). $SeRP_{ribo}$ showed flat binding profiles with enrichment values near one across coding sequences, reflecting a uniform, nascent chain-independent NAC occupancy, as expected from its constitutive ribosome association via the ribosome-anchoring domain.[3,17,18,38,39] In contrast, $SeRP_{NC}$ revealed distinct enrichment peaks, indicating specific NAC interactions with nascent chains at defined translation stages. These observations demonstrate that while NAC is constitutively ribosome-bound, its selective interactions with nascent chains can be captured using $SeRP_{NC}$, providing an insight into the timing and specificity of NAC engagement during protein synthesis.

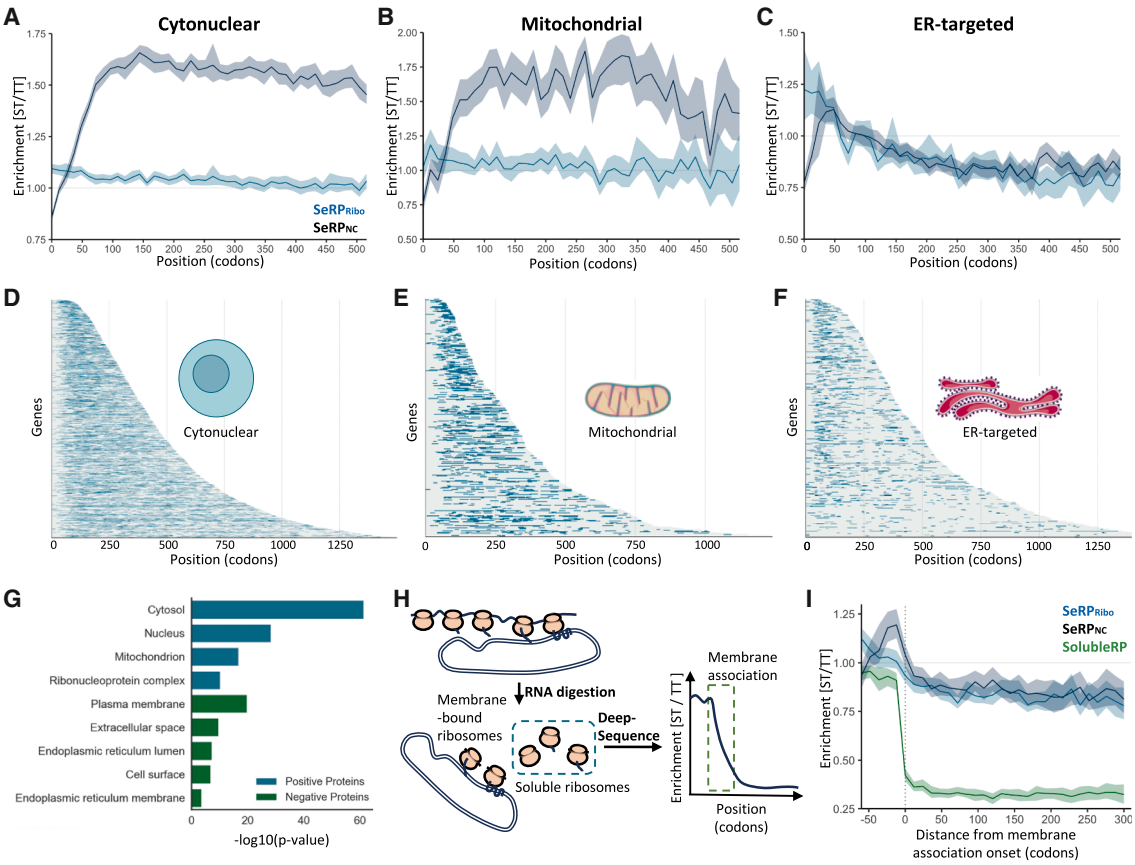

Figure 2. NAC binding patterns in nascent cytonuclear, mitochondrial, and ER-targeted proteins

(A–C) Metagene profiles of $SeRP_{NC}$ and $SeRP_{ribo}$ enrichments along coding sequences of cytonuclear, mitochondrial, and ER-targeted proteins. The metagenes include 6,824, 536, and 1,393 genes, respectively (coverage > 0.1 reads/codon). The shaded areas indicate 95% confidence intervals.

(D–F) Heatmaps of nascent chain-dependent NAC binding periods in cytonuclear (D), mitochondrial (E), and ER-translocated (F) proteins (3,275, 316, and 515 genes, respectively).

(G) Gene ontology analysis by cellular component of NAC-positive and NAC-negative proteins.

(H) Schematic of the SolubleRP pipeline for detection of co-translational membrane association.

(I) Metagene profile of $SeRP_{ribo}$, $SeRP_{NC}$, and SolubleRP enrichment aligned to the onset of membrane association in high-confidence co-translationally translocated proteins. The shaded areas indicate 95% confidence intervals.

See also Figures S2 and S3 and Tables S1, S2, S3, and S4.

To ensure that the $SeRP_{NC}$ data were not biased by lysine content, we compared NAC enrichments with lysine distribution and found no correlation (Figures 1B, 1C, and S1G–S1I). Regions with a high lysine density, such as the interdomain linker of G3BP2 and the C-terminal tail of RPL4 (red bars in Figures 1B and 1C, respectively), showed no significant NAC binding. Subsequent metagene analyses (see below) confirmed that lysine content is not a confounding factor (Figures S1J–S1M), indicating that DSP crosslinking effectively stabilized NAC interactions with nascent chains without bias.

NAC binding varies across cytonuclear, mitochondrial, and ER-targeted proteins

To study NAC's association with translating ribosomes, we performed metagene analyses on the $SeRP_{ribo}$ and $SeRP_{NC}$ datasets. Given NAC's roles in ER translocation and mitochondrial import,[3,15,16,41–43] nascent proteins were categorized by cellular location: (1) cytonuclear proteins (nucleus and cytoplasm); (2) ER-targeted proteins (ER lumen, ER membrane [ERM], and plasma membrane [PM]); and (3) mitochondrial proteins (matrix, intermembrane space, and membrane).

In the $SeRP_{ribo}$ dataset, metagene profiles for cytonuclear and mitochondrial proteins showed a uniform NAC enrichment across coding sequences (CDS) (Figures 2A and 2B), confirming NAC's nascent chain-independent binding and in agreement with the individual examples described above (Figures 1B, 1C, and S1G–S1I). Conversely, the $SeRP_{NC}$ dataset revealed a nascent chain-dependent binding pattern (Figures 2A and 2B) with minimal interactions early in translation, followed by a steady increase that plateaus after the synthesis of approximately 70 residues. Over 70% of nascent cytonuclear and mitochondrial proteins had at least one high-confidence NAC binding period, classifying them as NAC interactors (Table S1). Testing the lysine content within the 60 residues exposed at the

ribosomal surface at the onset of NAC binding periods showed a slight enrichment in lysine content as compared with randomly sampled positions (Figures S1J and S1K), suggesting that some NAC binding periods may be missed due to the limited crosslinkable sites. However, the lysine content did not correlate with the enrichment values (Figures S1J and S1K), confirming that NAC enrichments are largely independent of lysine abundance. Together, these data confirm that NAC ubiquitously associates with ribosomes translating cytonuclear and mitochondrial proteins.

In contrast, ER-targeted RNCs exhibited a length-dependent depletion in the $SeRP_{ribo}$ dataset, indicating NAC dissociation as translation progresses (Figure 2C). In the $SeRP_{NC}$ dataset, NAC binding increased as nascent chains emerged from the tunnel exit, peaking around residue 50 before decreasing. ER-targeted proteins showed fewer NAC binding periods, biased toward shorter nascent chains compared with cytonuclear and mitochondrial proteins (Figures 2D–2F). Cytonuclear and mitochondrial proteins also had longer NAC binding (median 26 codons) than ER-targeted proteins (median 20 codons; Figure S2A). Only 43% of the nascent ER-targeted proteins were classified as NAC interactors (Table S1). Gene Ontology (GO) analysis confirmed this localization dependency, with non-interactors enriched for ER-targeted proteins and interactors for cytonuclear and mitochondrial categories (Figure 2G).

The NAC interactome for ER-targeted proteins suggests that NAC can initially associate with nascent chains but is displaced during co-translational ER translocation (Figure 2C). We confirmed this using SolubleRP, an adaptation of ribosome profiling that infers ER translocation from ribosome depletion in the soluble fraction of a cellular lysate after nuclease digestion (Figure 2H). SolubleRP revealed a nascent chain-dependent depletion of soluble monosomes translating ER-targeted proteins (Figure S2B). The onset of membrane targeting for a set of high-confidence co-translationally ER-targeted substrates (Table S2) strongly correlated with the emergence of signal peptides (SPs) and transmembrane domains (TMDs) (Figure S2C). Aligning the $SeRP_{ribo}$ and $SeRP_{NC}$ datasets to the onset of membrane association revealed that NAC binds nascent chains prior to membrane targeting but rapidly dissociates thereafter (Figure 2I). This *in vivo* observation aligns with the previous reports of NAC's participation in SRP-mediated targeting, based on stalled RNCs *in vitro*.[3] The metagene analysis was supported by individual examples, including the secreted protein beta-2-microglobulin (B2M) and multi-pass membrane proteins tetraspanin 3 (TSPAN3) and delta(4)-desaturase sphingolipid 1 (DEGS1) (Figure S2D). To further evaluate NAC's involvement in ER targeting, we examined its binding relative to SP and TMD emergence. NAC binding periods coincided with the exposure of 25% and 45% of co-translationally targeted SPs and TMDs, respectively (Figures S2E and S2F). However, SPs and TMDs bound or unbound by NAC showed no significant differences in overall physicochemical properties, even when the 15-residue N termini to TMDs, which would also be NAC-accessible, were included (Figures S2G and S2H). Thus, while NAC binding is prevalent among co-translationally targeted SPs and TMDs, it was not universal.

NAC has also been proposed to mediate nascent chain recruitment to the mitochondrial surface.[16,41–43] Unlike ER-targeted proteins (Figures 2C and 2F), NAC binding to nascent mitochondrial proteins showed only a modest decrease during translation (Figures 2B and 2E), in agreement with mitochondrial precursors being primarily synthesized in the cytosol.[44] To investigate NAC's involvement in mitochondrial import, we analyzed its binding to cleavable mitochondrial targeting sequences (MTSs), which direct the import of inner mitochondrial membrane (IMM), intermembrane space, and matrix proteins. 30% of the analyzed MTSs were bound by NAC upon their emergence from the ribosomal tunnel exit (Figure S3A). Notably, proteins with NAC-bound MTSs were enriched in IMM proteins (p value < 0.05, cellular component GO enrichment), with 45% of IMM-targeted MTSs and 24% of matrix-targeted MTSs showing a NAC association (Table S3). Driven by this observation, we analyzed NAC binding to TMD-containing mitochondrial proteins in more detail, including IMM and outer mitochondrial membrane (OMM) proteins. NAC binding periods coincided with TMD emergence from the exit tunnel in both OMM and IMM proteins (Figure S3B; Table S4), predominantly in polytopic membrane proteins (Figure S3D). NAC-bound TMDs showed no significant differences in their physicochemical properties (Figure S3C). In support of the functional relevance of these interactions, the polytopic OMM proteins translocator protein (TSPO) and FUN14 domain-containing protein 1 (FUNDC1) (enrichment profiles in Figures S3E and S3F), whose mitochondrial import is impaired upon NAC depletion,[45] were included in the NAC-bound group (black arrows; Figure S3B). In contrast, the tail-anchored proteins CDGSH iron-sulfur domain-containing protein 1 (CISD1) and mitochondrial antiviral signaling protein (MAVS) (red arrows), which are unaffected by NAC depletion, were not bound. The TSPO enrichment profile revealed a single, specific NAC binding event at the second emerging TMD (Figure S3E), suggesting that NAC's role in TSPO import is limited to a short-lived interaction with a defined TMD. Overall, our data support a role for NAC in the biogenesis of both IMMs and OMMs, extending its previously reported involvement in OMM biogenesis.[45]

In summary, our profiling provides a proteome-wide view of NAC interactions with cytonuclear, mitochondrial, and ER-targeted proteins, with cytonuclear and mitochondrial proteins representing its primary substrates.

NAC recognizes emerging domains of cytonuclear proteins

We next investigated the functional significance of NAC binding to nascent cytonuclear proteins. Given that NAC binding often coincided with the emergence of annotated protein domains in individual examples (Figures 1B, 1C, and S1G–S1I), we examined this correlation at a proteome-wide scale. Across the proteome, emerging cytonuclear protein domains showed increased NAC interactions compared with flanking regions (Figure 3A), a pattern also observed in mitochondrial proteins (Figure 3B) but not in ER-targeted proteins (Figure S4A). Metagene NAC binding profiles showed a sharp increase at the beginning of domain exposure, followed by a gradual decline as the domain is further translated. Notably, nascent chains with early

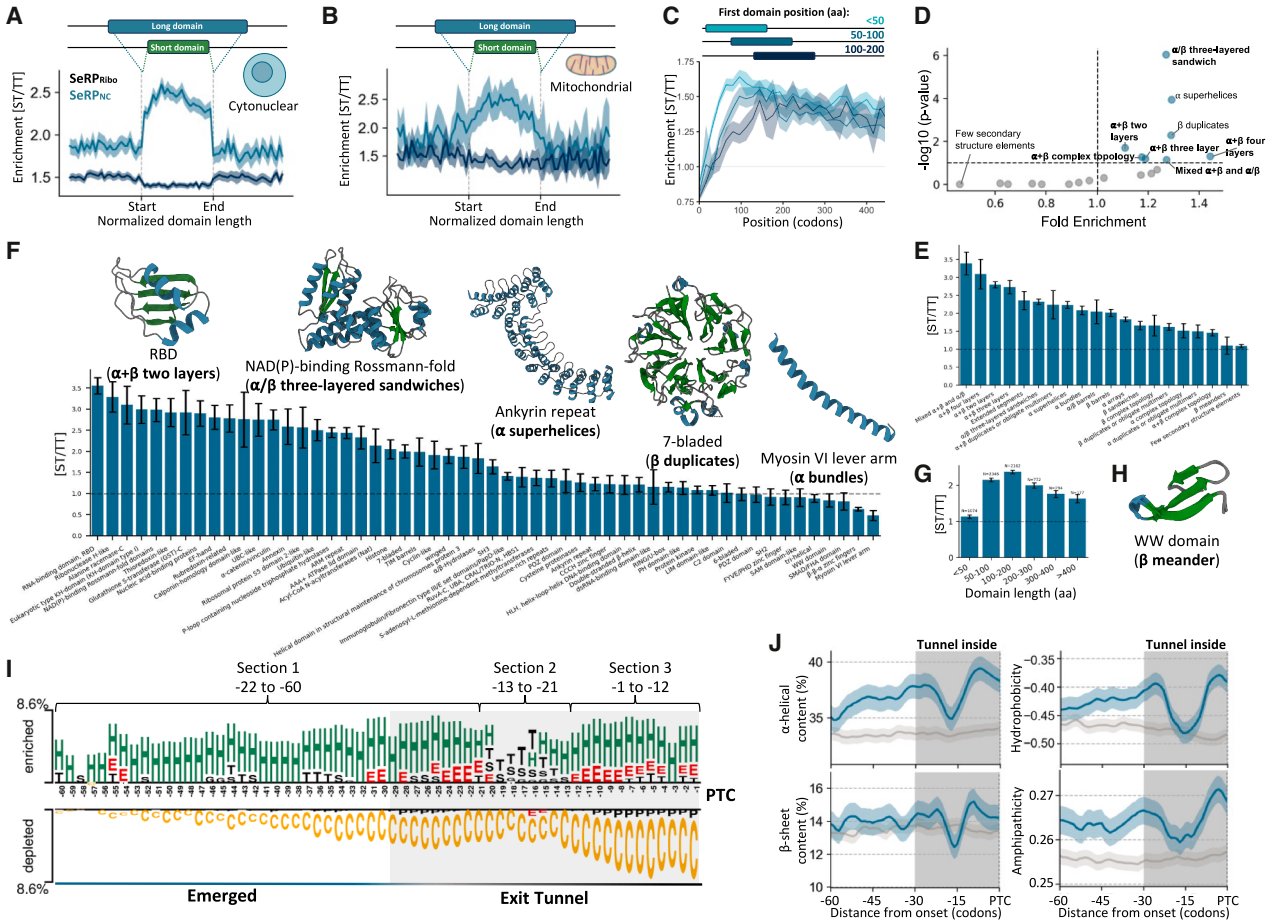

Figure 3. Molecular determinants of NAC binding to cytonuclear and mitochondrial nascent chains

(A and B) Length-normalized ST/TT enrichment within domains and flanking regions for cytonuclear (A) and mitochondrial (B) proteins for $SeRP_{ribo}$ and $SeRP_{NC}$.

(C) Metagene profiles grouped by position of the most N-terminal domain (<50, 50–100, and 100–200 residues; 3,250, 1,115, and 805 proteins, respectively).

(D) Frequency enrichment of domains containing at least one NAC binding period.

(E and F) Total ST/TT enrichment across evolutionary classification of protein domains (ECOD) domain architectures (E) and topologies (F); underrepresented topologies (<20 proteins) were excluded. The representative structures are shown (PDBs: 8csv, 1hd0, 1a4i, 1oe9, and 1i2m). Error bars indicate the standard error of the mean (SEM).

(G) Total ST/TT enrichment as a function of domain length. Error bars represent SEM.

(H) Example of a β-meander domain (PDB: 1ywj).

(I) Position-specific enrichment of DSSP secondary structure in the ribosome-proximal 60 residues at NAC binding onset in cytonuclear proteins. The annotation follows DSSP classes: H, helix; E, strand; T, turn; S, bend; C, coil; G, 3_{10}-helix; and P, pi-helix.

(J) Metagene profiles of secondary structure (DSSP annotated from AlphaFold structures), hydrophobicity (Kyte-Doolittle),[46] and amphipathicity (measured as the hydrophobic moment of the helix[47]) aligned to NAC binding onset. The gray line indicates a randomized background. The shaded areas indicate 95% confidence intervals.

See also Figure S4.

emerging domains exhibited earlier NAC binding (Figure 3C), emphasizing the correlation between domain emergence and NAC engagement. In agreement, nascent chains accessible to NAC at the tunnel exit during the binding periods showed features correlated with folding domains, including a high hydrophobicity, aromatic content, α-helical and β-sheet structures, reduced predicted disorder, and lower accessible surface area (ASA) (Figure S4B). This suggests that NAC binds elements destined to be buried in the final structure. Long disordered regions had fewer NAC binding peaks (Figures 1B, 1C, and S1G–S1I), a trend also seen in non-globular and coiled-coil proteins lacking folded domains (Figures S4C and S4D).

NAC binding profiles varied strongly between domains, showing differences in the number of binding peaks within a single domain (Figures 1B, 1C, and S1G–S1I), prompting an analysis of specific domain architectures linked to NAC binding (Figure 3D). NAC-bound domains were enriched in mixed α and β architectures, α superhelices, and β duplicates compared with other domain architectures. Local NAC enrichment within domains mirrored this trend, with strong NAC

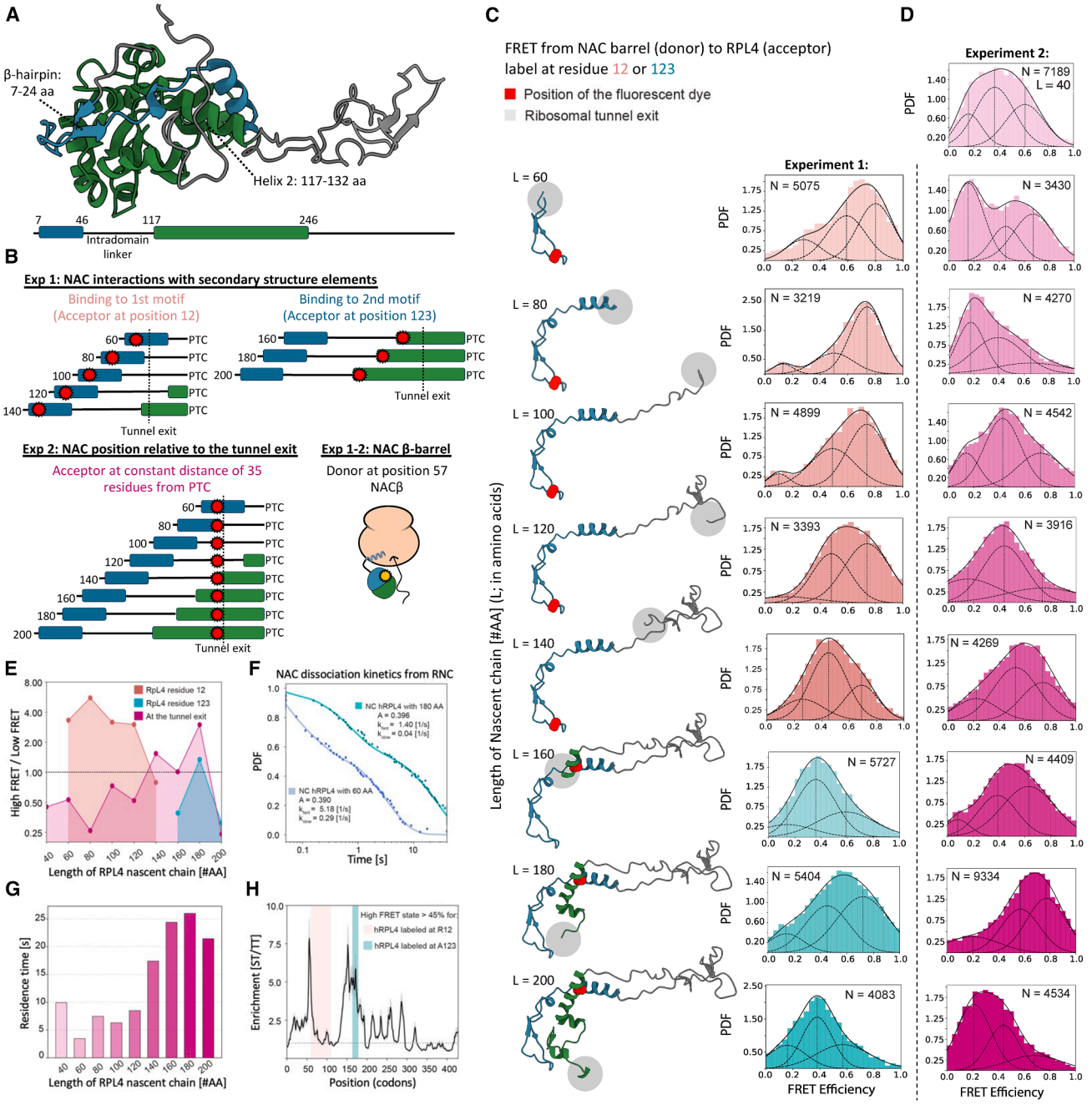

Figure 4. smFRET analysis of NAC interaction with ribosomes and RPL4 nascent chains

(A) AlphaFold model showing the RPL4 globular domain. The blue and green colors indicate the N- and C-terminal segments of the RPL4 globular domain, respectively.

(B) Schematic of fluorophore positions on RPL4 nascent chains of different lengths.

(C) smFRET histograms for NAC β-barrel donors paired with acceptor dyes (red dots) at RPL4 residues 12 (L = 60–140) or 123 (L = 160–200). The corresponding AlphaFold models of exposed RPL4 segments are shown; the gray sphere indicates the position of the ribosome tunnel exit.

(D) smFRET histograms for NAC β-barrel donors paired with an acceptor dye at the ribosome exit tunnel. In (C) and (D), the histograms were fitted with three Gaussians; the mean FRET values are reported in Table S5.

(E) Summary of the distribution of NAC in high FRET populations at different nascent chain lengths for the FRET pair with the acceptor dye at RPL4 residue 12 (salmon), RPL4 residue 123 (teal), and at the ribosome exit tunnel (pink). The number of molecules with FRET > 0.6 is summed and divided over that with FRET < 0.4.

(legend continued on next page)

binding to mixed α and β architectures (Figure 3E). α superhelices were the main α architecture bound by NAC, while β duplicates showed lower enrichment values. Domains with minimal secondary structure elements were notably depleted in NAC binding (Figures 3D and 3E). Examining NAC preferences for domain topologies revealed a similar trend (Figure 3F), with domains like RNA-binding domains (RBD; α + β two-layered architecture) and a NAD(P)-binding Rossmann-fold (α/β three-layered sandwiches) showing strong NAC binding, while myosin VI lever arm (α-bundles) and WW domains (β-meander) showed reduced binding. NAC binding, enrichment, and topology preferences show no correlation with lysine content in domains (Figures S1L and S1M), indicating that the observed domain preferences (Figure 3F) are not driven by lysine-dependent crosslinking.

Overall, these findings suggest a role of NAC in the biogenesis of folded domains, congruent with NAC being a co-translationally acting chaperone. NAC binding varies across domain architectures, indicating an evolutionarily selected chaperone activity. Mixed α/β domains show stronger NAC association, likely reflecting their greater topological complexity and folding demands, whereas small domains (<50 residues) with low folding complexity exhibit weaker binding, including Src homology domain 2 (SH2) (α + β two-layers), tri-helical (α-arrays), β–β–α zinc fingers (few secondary structures), and WW domains (β--meander) (Figures 3G and 3H).

If NAC indeed supports early domain folding during translation, its loss would be expected to compromise cytosolic proteostasis. Accordingly, rapid depletion of NACβ using an auxin-inducible degron system[48] resulted in a selective activation of the cytosolic heat shock response, as evidenced by an increased translation of heat shock response chaperones (Figure S4E), prior to detectable effects on ER or mitochondrial proteostasis. NAC depletion also increased the translation of NAC's co-translational substrates (Figure S4F), which is consistent with a compensatory upregulation in response to impaired folding assistance.[49–51] Gene ontology analysis revealed that significantly upregulated proteins (Figures S4G and S4H) were enriched for cytonuclear categories, heat shock response functions, and domains that are among those preferentially bound by NAC (e.g., RNA-binding domains and NAD(P)-binding Rossmann-fold). Together, these findings point to NAC as an early-acting co-translational chaperone that safeguards cytosolic proteostasis.

Molecular determinants of NAC binding to cytonuclear proteins

We next analyzed the physicochemical features of nascent cytonuclear proteins at the onset of NAC binding. Position-specific analysis of AlphaFold-based Dictionary of Secondary Structure of Proteins (DSSP) annotations in the 60 most recently translated residues revealed an enrichment of both α- and β-secondary structures, along with a concomitant reduction in disorder relative to a randomized control, consistent with NAC engagement of folded domains (Figure 3I). Particularly, NAC binding coincided with the synthesis of secondary structure elements, separated by short connecting loops (section 2 in Figure 3I). Although these elements are initially buried within the ribosomal exit tunnel, they become partially or completely exposed during the binding period. Exploring the physicochemical properties of these segments at the metagene level revealed that NAC binding coincides with the emergence of regions enriched in hydrophobicity, α-helical propensity, and amphipathic characteristics (Figures 3J and S4I). β-sheet enrichment was lower, indicating that hydrophobicity and helical propensity are the primary binding criteria. A similar position-specific analysis of primary sequences did not yield a sequence-specific binding motif (Figure S4J), but amino acid compositions aligned with the observed secondary structure propensities.

Thus, NAC binding appears to be guided by nascent chain conformation rather than sequence, consistent with broad substrate binding. It engages secondary structure motifs connected by short loops, suggesting preferential binding to regions destined to form well-folded structures and in agreement with reduced binding to extended helices or coiled-coil regions (Figures 3F and S4D). Overall, data suggest that NAC facilitates the biogenesis of minimal tertiary folds composed of (α/β)-loop-(α/β) motifs.

Direct observation of dynamic NAC interactions with nascent chains

To dissect the mechanism of NAC interactions with emerging nascent chains, we performed *in vitro* smFRET using total internal reflection fluorescence microscopy (TIRFM) (Figure S5A). RPL4 was selected as a model substrate (Figures 4A and S5B), as it allows the generation of stalled RNCs via *in vitro* translation, and the structure of NAC-bound ribosomes translating Ribosomal protein L4 (RPL4) is available.[4] RPL4 contains an N-terminal globular domain that adopts an α/β three-layered sandwich architecture (Figure 4A), with two segments separated by an extended intradomain linker. Our SeRP data indicate that NAC binds both RPL4 segments but not the linker (Figure 1C).

To directly observe NAC β-barrel interactions with the ribosome and nascent chain and to understand whether they compete or cooperate, we labeled RNCs with the acceptor dye Atto647N at various positions in the nascent chain (Figure 4B) and immobilized them on imaging slides via a biotin moiety at the 5′ end of the mRNA (Figure S5A). NAC was labeled with the donor dye Cy3B at residue 57 in the β-barrel domain. To probe the interaction of NAC with the two segments in the RPL4 globular domain (experiment 1), Atto647N was incorporated at residue 12 or 123 of RPL4 (Figures 4B and 4C). To probe the position of the NAC β-barrel domain relative to the exit tunnel (experiment 2), Atto647N was incorporated at a defined distance

(F) Representative kinetic traces of NAC dissociation from RPL4 RNCs (60 and 180 residues). The dwell time distribution data were fitted to the sum of two exponential functions, which gave the dissociation rate constants for the fast- and slow-dissociating populations (k_{fast} and k_{slow}) and the fraction of the fast-dissociating population (A).

(G) Residence times of the slowly dissociating NAC population as a function of the nascent chain length.

(H) Nascent chain lengths showing NAC interactions mapped onto the NAC interaction profile of RPL4.

See also Figures S5 and S6.

of 35 residues from the nascent chain C terminus, ensuring equivalent positions across the RNCs with varying nascent chain lengths (Figures 4B and 4D). NAC binding to immobilized RNCs was assessed via fluorescence colocalization and FRET between the dye pair under TIRFM (Figures S5A and S6), and the kinetic stability of NAC-RNC interactions was measured based on the interaction lifetime (Figure S5A).

Hidden Markov modeling (HMM) of smFRET traces revealed three FRET states, with low, medium, and high FRET efficiencies, for all FRET pairs (Figures S5C, S5D, and S6). High FRET efficiencies in experiment 1 indicate interactions between the NAC β-barrel domain and the labeled motif. In experiment 2, the high FRET state is assigned to ribosome docking of the NAC β-barrel near the exit tunnel,[3] whereas medium/low FRET states reflect dissociation, remaining either free or engaging in alternative interactions. At a nascent chain length of 40 residues, only the N-terminal ~5 residues of RPL4 have emerged from the exit tunnel; this histogram serves as a "baseline" for NAC barrel distribution at the exit tunnel (experiment 2) in the absence of significant nascent chain interactions.

As the RPL4 nascent chain elongates, changes in smFRET distributions indicate two stages of interaction between the NAC β-barrel and the nascent chain. The first interaction peaked at nascent chain lengths of 60–80 residues, as indicated by a dominance of a high FRET state with the acceptor dye at RPL4 residue 12 (experiment 1) and a low FRET state with the acceptor dye at the tunnel exit (experiment 2) (Figures 4D, 4E, and S5F). The anti-correlation of these two FRET pairs (Figure 4E) suggests that the β-barrel domain moved away from the ribosome due to competing interactions with the nascent chain. As the nascent chain elongates, the high FRET population with the probe at RPL4 residue 12 (experiment 1) decreased until it became a minor state at 140 residues (Figures 4C, 4E, and S5E), indicating the dissolution of NAC interaction with this N-terminal region.

The second stage of interaction occurred when the nascent chain exceeded 160 residues, marked by an increased kinetic stability of the NAC-RNC interaction (Figures 4F and 4G). In agreement with previous reports,[45] NAC displayed biphasic dissociation kinetics from the RNC at a nascent chain length of 60 residues (rate constants: 0.29 and 5.2 s^{-1}) (Figure 4F). While the population distributions and the stability of the fast-dissociating population varied modestly with chain lengths (Figures S5G–S5I), the lifetime of the slow-dissociating population increased from 4–10 s to ~25 s at lengths exceeding 160 residues (Figures 4F and 4G), indicating enhanced NAC-RNC interactions. At a nascent chain length of 180 residues, the high FRET states were prominent in both smFRET histograms of experiments 1 and 2 (Figures 4C–4E). These results strongly suggest that favorable NAC interactions with both the ribosome surface and the RPL4 nascent chain contribute to the enhanced NAC-RNC stability.

Collectively, the smFRET data show that the NAC β-barrel domain dynamically interacts with defined RPL4 regions at specific stages of translation. These interactions can modulate the position of the NAC β-barrel at the ribosomal exit tunnel, either displacing it or bringing it into closer proximity. The two detected NAC interaction regions on the RPL4 nascent chain agreed well with the $SeRP_{NC}$ data (Figure 4H). Because these smFRET experiments were performed on purified complexes without other cellular factors, this agreement indicates that NAC's preference for nascent chain features does not rely on other factors. The longer NAC interactions with RPL4's N-terminal region observed in smFRET compared with SeRP likely result from competition with other cellular factors *in vivo* leading to earlier release. In agreement with this possibility, the intradomain loop of RPL4 is co-translationally bound by a specific chaperone in yeast.[52]

Structural insights into NAC interaction with nascent chains

To understand the molecular basis of NAC binding to nascent chains, we determined the structure of NAC in complex with the RPL4 RNC using cryo-EM (Figure 5A). While previous studies have determined NAC-RNC structures in complex with different ribosome-associated factors,[2–4,13,53] direct interactions between NAC and nascent chains have not been observed. We generated stalled RNCs containing the first 158 amino acids of RPL4 followed by the unspliced X-box binding protein 1 (XBP1u) arrest peptide, yielding a comparable exposed nascent chain as the 180-residue RPL4 RNC used in smFRET experiments, where maximal kinetic stability was observed.

The cryo-EM map shows NAC bound at the polypeptide tunnel exit of RPL4 RNCs at the same position as described previously (Figure 5B),[3,4] with the N-terminal basic ribosome anchor of NACβ bound at eL19 and eL22, and two positively charged α-helices of the NAC β-barrel domain contacting rRNA. The nascent polypeptide chain could be traced throughout the exit tunnel (Figure 5C). Additionally, we observed a continuation of the nascent chain density outside the tunnel exit at lower thresholds (Figure 5D). The extra density was observed along the 28S rRNA lining the polypeptide exit tunnel and contacted 5.8S rRNA on the surface of the ribosome, as well as the entrance to the NAC β-barrel. This surface of NAC presents a patch of hydrophobic residues, which are contributed by both NACα and NACβ, including NACα I128 and NACβ V53 and L83, at a short distance from the tunnel exit (Figures 5E, S7A, and S7B).

The location of the nascent chain density outside the tunnel exit was reproducible in two independently obtained cryo-EM maps (Figure S7C) and was absent in previous studies using shorter RPL4 chains[4] and other nascent chains.[2,3,13,53] Consistent with a stabilizing interaction between NAC and the nascent chain, the classification for the conformation of the NAC globular domain revealed a more defined nascent chain density outside the exit tunnel (Figure 5D) compared with the map prior to classification (Figure S7C). The accumulation of nascent chain density near the NAC β-barrel is consistent with the smFRET measurements and $SeRP_{NC}$ enrichment. This enrichment may be explained by multiple NAC lysine residues positioned within the DSP spacer length (12Å) (Figure S7D).

To test the role of the hydrophobic patch of the NAC β-barrel domain, we mutated the hydrophobic residues at this surface (NAC_{mut}; NACα I128N, NACβ V53S, and L83N) and analyzed NAC interactions with the nascent chain and the tunnel exit by smFRET, reproducing experiments 1 and 2 using the 180-amino acid RPL4 RNC. Pairing a donor dye in NAC_{mut} with acceptor dyes at RPL4 residue 123 or the ribosome exit tunnel nearly abolished the high FRET population in both setups, and the low FRET population increased over four-fold

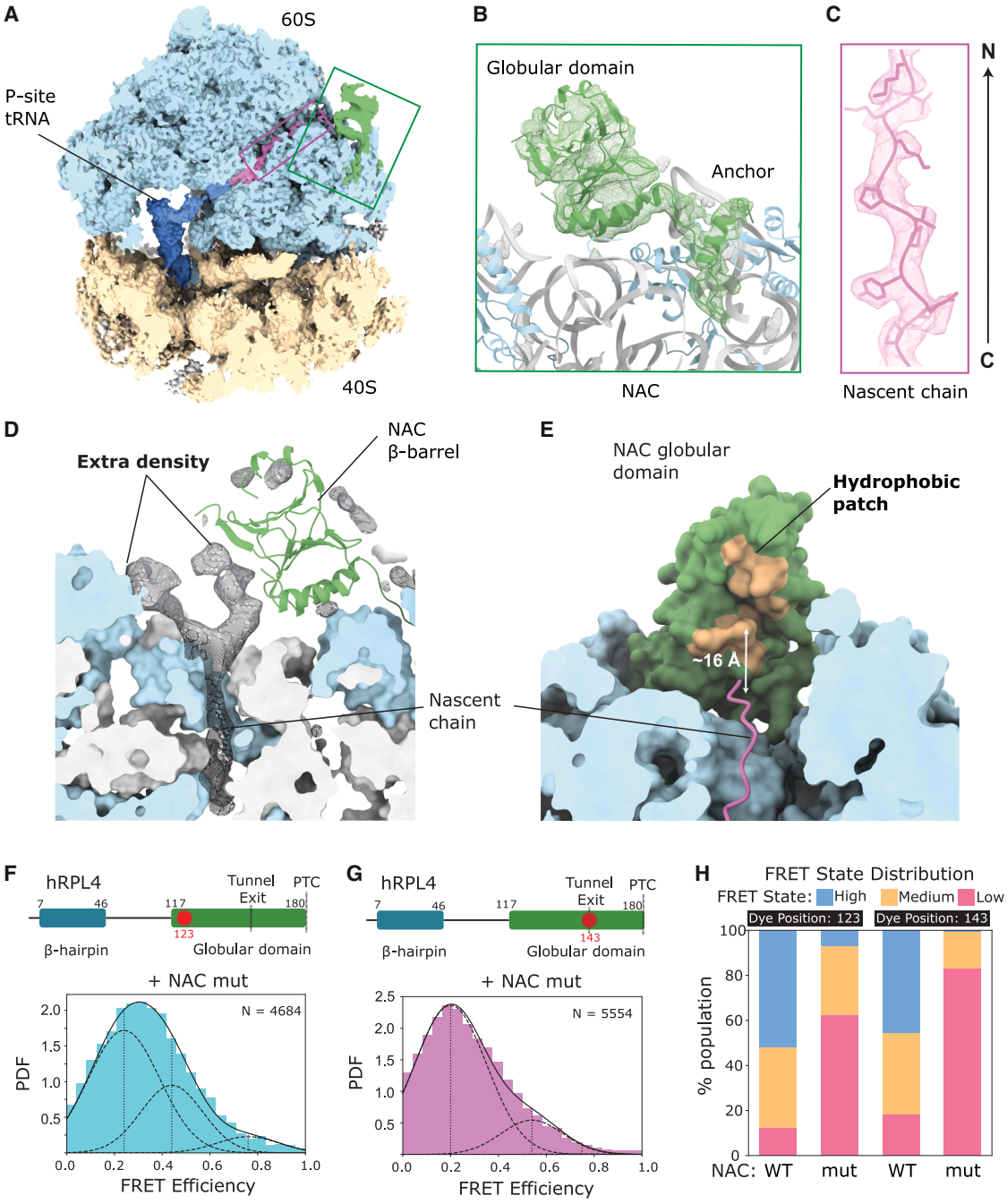

Figure 5. Structural analysis of RPL4 RNC complexes with NAC

(A) Cross section of the cryo-EM map, low-pass filtered to 4 Å. The rectangles indicate views in (B) and (C).

(B and C) Close-up views of NAC (B) and nascent chain in the exit tunnel (C). The difference density between the cryo-EM map and the 80S model (mesh) was low-pass filtered to 4 Å (B) or unfiltered (C).

(D) Continuation of the nascent chain density outside the exit tunnel. The difference density between the cryo-EM map and the 80S/NAC model was low-pass filtered to 6 Å and is shown as a mesh. The 60S proteins are in blue; rRNA in gray.

(E) Bottom view of the NAC β-barrel highlighting the hydrophobic patch and its distance to the exit tunnel.

(F and G) smFRET histograms for mutant NAC β-barrel donor paired with acceptor dyes at RPL4 residue 123 (F) or the tunnel exit (G).

(H) Quantification of FRET state populations in (F and G).

See also Figure S7 and Table S6.

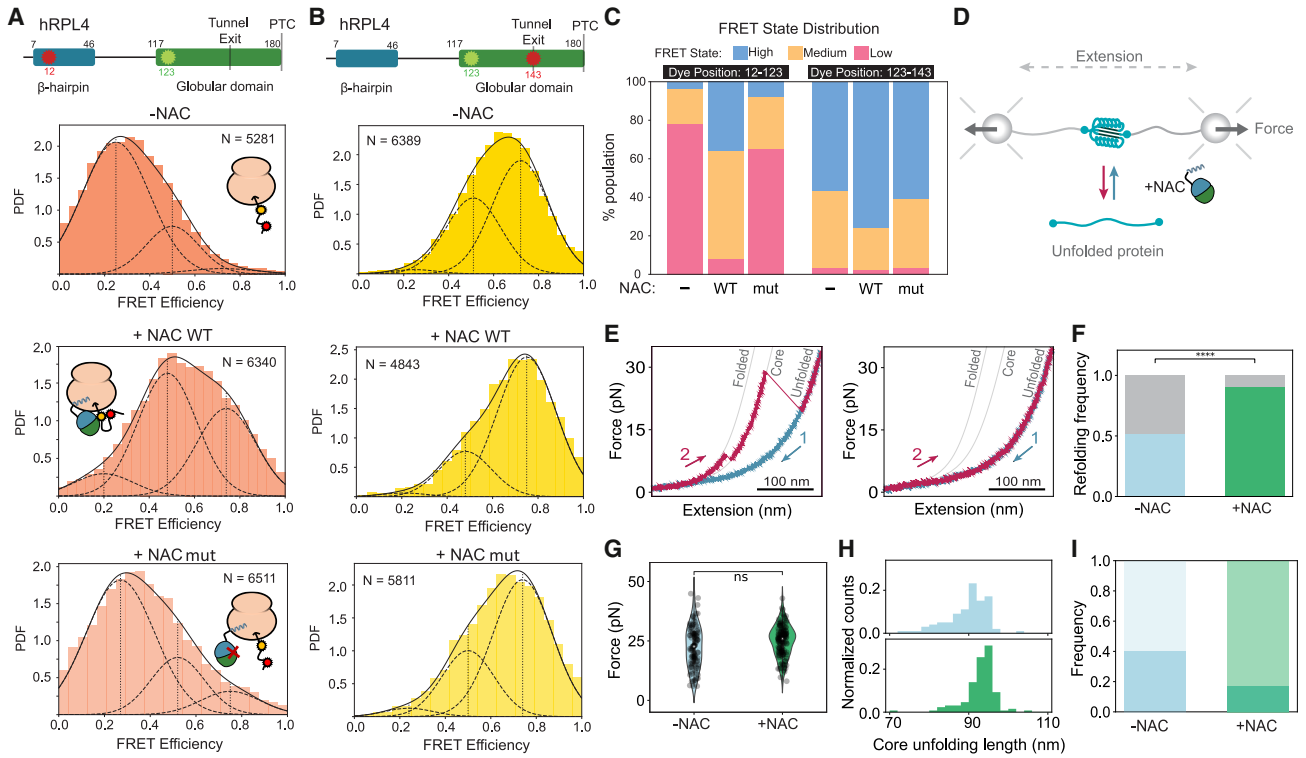

Figure 6. Single-molecule analyses of NAC chaperoning activity

(A and B) smFRET histograms for RPL4 dye pairs in the absence or presence of wild-type NAC or NAC_{mut}. Data were fitted with three Gaussians; the mean FRET efficiencies of the individual FRET states are reported in Table S5.

(C) Quantification of FRET populations for dye pairs at RPL4 residues 12–123 (A) and 123–143 (B).

(D) Schematic of the optical tweezers assay.

(E) Representative force-extension curves of folded (left) and unfolded MBP (right) in the absence of NAC. Following the relaxation of unfolded MBP molecule (1) and waiting at 0 pN for 5 s, the stretching curve (2) displays a large step corresponding to unfolding of the MBP core. The gray curves are worm-like chain (WLC) fits.

(F) Refolding frequency of MBP cores in the absence and presence of NAC (5 μM). *N* (cycles) are 193 (14 molecules) and 147 (17 molecules) without and with NAC. **** indicates a significant difference ($p < 0.0001$) from a one-tailed two-proportion Z-test.

(G and H) Unfolding forces (G) and unfolding lengths (H) of refolded MBP cores with and without NAC. No significant differences in the unfolding forces were observed (Mann-Whitney test). The unfolding length of refolded core structures had mean values of 90.1 ± 5.8 nm (SD, $N = 98$) and 91.1 ± 11.5 nm (SD, $N = 130$), respectively. The histograms are normalized to the total number of states analyzed per condition.

(I) Frequency of small (70 to 90 nm) and large (larger than 90 nm) MBP core structures in the absence and presence of NAC. The frequencies of small unfolds in the absence and presence of NAC are significantly different ($p < 0.00001$ from a one-tailed two-proportion Z-test).

See also Figure S8.

compared with wild-type NAC (Figures 5F–5H). These results indicate that the hydrophobic patch mediates nascent chain engagement and suggest that these contacts drove close positioning of the NAC β-barrel at the tunnel exit.

NAC induces nascent chain folding at the ribosomal tunnel exit

To directly assess NAC's influence on nascent chain folding, we measured the intramolecular FRET of the 180-residue RPL4 nascent chain, using fluorophore proximity as a proxy for compaction and folding. The RPL4 nascent chain was labeled with Cy3B (donor) and Atto647N (acceptor) at two pairs of positions, 12–123 and 123–143 (Figures 6A and 6B). Doubly labeled RNCs were optically selected, and FRET efficiency was measured using the smTIRFM setup. The presence of NAC significantly increased the population of nascent chains in the high FRET state with both pairs of FRET probes (Figures 6A and 6B). This effect is especially prominent with the 12–123 dye pair: without NAC, the smFRET histogram was dominated by a low FRET population indicating an expanded nascent chain, whereas the medium (~55%) and high (nearly 40%) FRET states became dominant upon the addition of NAC (Figures 6A and 6C). These results indicate that NAC induces a long-range compaction of the nascent chain, which brings the N- and C-terminal segments of the RPL4 globular domain into close proximity (Figure 4A). In agreement, the increased proximity of the 123–143 pair indicates NAC-induced local compaction of the C-terminal segment near the ribosomal tunnel exit (Figures 6B and 6C). The ability of NAC to remodel the RPL4 nascent chain was largely abolished with NAC_{mut} (Figures 6A–6C), confirming that this activity is dependent on the identified hydrophobic patch.

These data provide direct evidence that NAC exerts a chaperoning activity on the RPL4 nascent chain at the ribosome. They further show that the NAC β-barrel domain, despite its limited interaction surface, is sufficient to nucleate folding and promote long-range compaction of the nascent protein.

Principles of NAC chaperoning activity

To mechanistically dissect NAC's chaperoning activity, we used optical tweezers to examine how NAC influences the folding of a free polypeptide chain at the single-molecule level. We employed maltose-binding protein (MBP), a mixed α/β protein, as a well-established model for chaperone-assisted folding.[54] MBP has been extensively characterized in tweezer experiments with other co-translational chaperones, including trigger factor (TF), DnaK/Hsp70, and GroEL,[55–57] providing a robust benchmark to understand the molecular basis of NAC chaperoning.

We first assessed MBP folding efficiency in the absence or presence of NAC. Single MBP molecules were tethered between two laser-trapped polystyrene beads using DNA handles (Figure 6D; see STAR Methods). After mechanically unfolding the tethered protein by moving one bead away from the other, we subjected MBP to repeated cycles of relaxation (by bringing the beads together), waiting for 5 s in the absence of applied force to allow refolding, and stretching (by separating the beads again) (Figures 6D, 6E, and S8). The polypeptide chain either folded, showing unfolding of the MBP core during subsequent stretching (Figure 6E, left), or remained unfolded, as shown by a lack of unfolding features during stretching (Figure 6E, right).[58] Because formation of the MBP core state is the rate-limiting step in folding, we quantified the fraction of cycles showing MBP core formation. The presence of NAC heterodimers significantly enhanced the MBP core refolding frequency from 0.51 to 0.90 (Figure 6F), proving that NAC directly promotes the folding process.[57,59] NAC_{mut} failed to efficiently refold MBP (Figures S8D and S8E), confirming dependence on the same hydrophobic patch required for nascent chain folding (Figures 6A–6C).

We next analyzed MBP core states in the absence or presence of NAC (Figure 6E, left) for their mechanical stability and unfolding step size as a proxy of their structural nature. Force-dependent lifetimes (Figure S8F) and average unfolding forces (Figure 6G) showed no significant differences between conditions, indicating that similar core states form with or without NAC. Unfolding step sizes were also comparable, peaking near the theoretically expected length of 96 nm for the native core state (Figure 6H), implying that NAC promotes formation of the native fold. Importantly, unchanged unfolding forces indicate that NAC chaperoning activity does not rely on stabilizing final or intermediate states.

The core unfolding step-size distribution was narrower in the presence of NAC (Figure 6H), whereas in its absence, cores with smaller unfolding step sizes (70–90 nm) were about two-fold more frequent (Figure 6I). Incomplete core structures were less mechanically stable (Figures S8G and S8H), but the unfolding forces of the small and large cores were identical, indicating that NAC only changes their relative distribution. While we formally cannot discriminate if these "small cores" correspond to incomplete folding intermediates or misfolded states, their lower unfolding forces and lengths, which are close to (but smaller than) large cores, are consistent with states that have most but not all core structural features. Overall, the data show that NAC promotes the on-pathway formation of more complete and structurally homogeneous core states (Figures 6H, 6I, S8G, and S8H), either by lowering folding energy barriers or by limiting access to misfolded or incomplete states.

The NAC chaperoning functions are notable. First, it is unclear for most chaperones if they promote folding directly by increasing the folding probability or indirectly by limiting aggregation. As aggregation partners were absent in this experiment, NAC interactions directly promote folding transitions, similar to the ATP-driven chaperone GroEL-ES.[60] Second, several chaperones, including TF, DnaK, and GroEL, perform their function by binding and stabilizing partially folded intermediates, including the MBP core state.[55–57] In contrast, NAC promotes folding without stabilizing the intermediate tertiary structures, given that NAC did not cause increased unfolding forces (Figures 6G and S8G). This mechanism is consistent with our smFRET data and the notion that early and transient NAC binding to short emerging segments is sufficient to funnel nascent chains toward productive folding, as these interactions do not increase tertiary structure stability.

DISCUSSION

NAC is a central interaction hub at the ribosomal tunnel exit that coordinates the access of protein biogenesis factors to nascent chains,[2–4,11–15,39] but the nature and specificity of its interactions and their impact on early folding remain unclear. Here, we profiled the NAC co-translational interactome *in vivo* with ribosomes and nascent chains, defining its substrate pool and the nascent chain features recognized. Integrating single-molecule and cryo-EM approaches *in vitro*, we provide direct evidence of NAC's dynamic interaction with the emerging nascent chains, demonstrate its activity as a chaperone, and explore its working principles. These findings establish NAC as a general co-translational chaperone that promotes early folding events at the ribosomal vestibule.

Our SeRP data reveals that NAC is constitutively associated with ribosomes translating cytonuclear and mitochondrial proteins, with its β-barrel domain establishing transient and dynamic interactions with approximately 70% of these nascent chains during translation. These interactions are mediated by a ribosome-oriented hydrophobic patch in the NAC β-barrel domain that engages nascent chains emerging at the tunnel exit, particularly hydrophobic regions with an α-helical propensity and amphipathic character that are destined to form compact folded domains once all required residues become available. Through these interactions, NAC is capable of biasing the folding landscape toward native structure formation while suppressing misfolded conformations. This chaperone mechanism shows differences from known mechanisms such as shielding unfolded conformers as a "holdase" (e.g., small heat-shock proteins [HSPs], Hsp70), stabilizing folding intermediates (TF, Hsp70, Hsp90, and GroEL-ES), and confining the folding of unfolded polypeptides (GroEL-ES).[55–57,61,62]

Our data also show that NAC's chaperone activity is intrinsically dynamic. Interactions with nascent chains are regulated

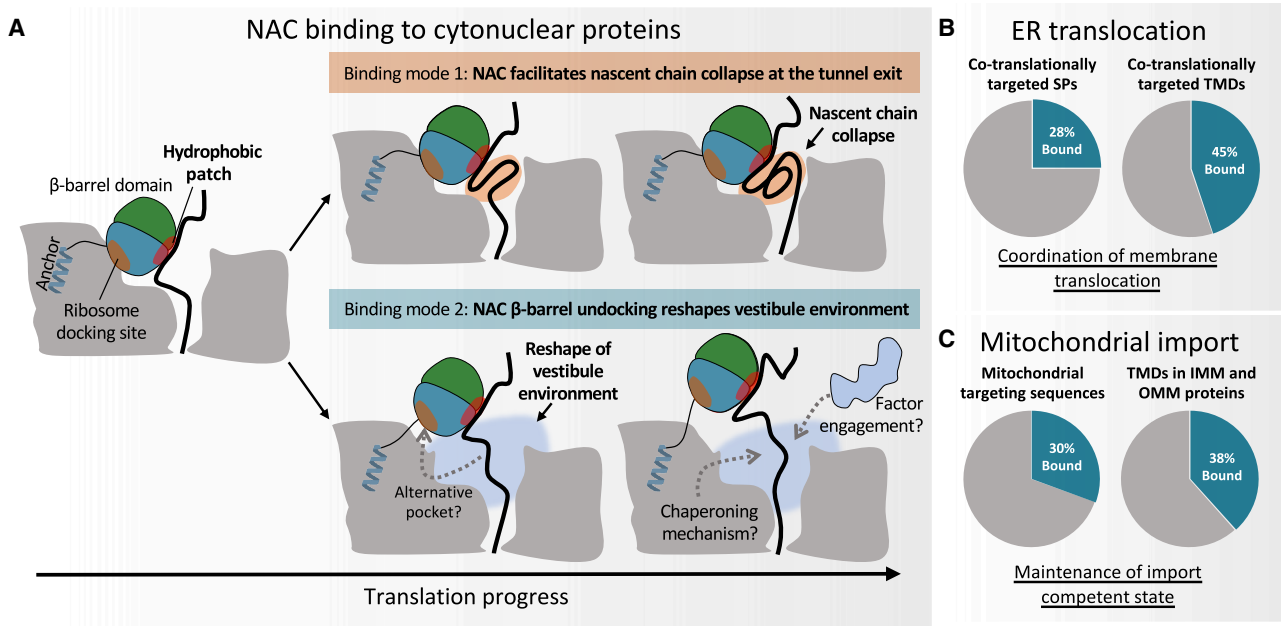

Figure 7. Roles of NAC in cytonuclear, mitochondrial, and ER protein biogenesis

(A) Model of NAC chaperone action on cytonuclear proteins, illustrating the two binding modes defined by β-barrel positioning and their effects on the vestibule environment and factor accessibility.

(B) NAC recognizes SP and, preferentially, TMDs in proteins co-translationally targeted to the ER.

(C) NAC binds certain MTSs and TMDs in mitochondrial IMMs and OMMs, suggesting a role in maintaining the translocation-competent state of mitochondrial precursors.

by chain length and sequence features and are accompanied by repositioning of the β-barrel domain relative to the tunnel exit. These movements dynamically reshape the vestibule environment as the nascent chain emerges, creating a multivalent environment defined by NAC's hydrophobic surface, its cationic surface, and the anionic ribosomal exit. Such context-dependent dynamics likely allow NAC to fine-tune the local thermodynamic landscape as translation proceeds (Figure 7A).

The ability of the NAC β-barrel domain to dynamically engage and disengage the ribosome and nascent chains also provides a framework for factor exchange at the tunnel exit (Figure 7A). Displacement of the β-barrel domain may facilitate a handover to downstream biogenesis factors; as shown for SRP,[3] NAC modulates its access upon signal peptide emergence, both by weakening β-barrel engagement with the ribosome and by exposing an additional surface for SP binding in NAC.[3] Thus, by modulating its position and nascent chain binding, NAC may act as a molecular switch that fine-tunes co-translational decisions, ensuring proper coordination between early folding events, membrane targeting, and potentially other co-translational processes.

Beyond cytonuclear proteins, NAC interacts with ER-targeted proteins and mitochondrial precursors. The binding patterns of NAC observed for ER-targeted proteins agree with its reported mechanism of action in SRP-mediated co-translational ER targeting[3] (Figure 7B). In mitochondrial precursors (Figure 7C), NAC binds to nascent folding domains, such as in cytonuclear polypeptides, and to some but not all MTS, leaving the functional significance of these interactions unclear. Hsc70 and Hsp90 co-chaperones can also bind certain MTS co-translationally to maintain import competence,[63] hinting that NAC may act similarly or help recruit such cytosolic factors. Additionally, NAC participates in mitochondrial membrane protein biogenesis by interacting with emerging TMDs of OMM and IMM proteins (Figure 7C), which utilize distinct import pathways, presumably for transient shielding of these hydrophobic segments from aggregation. While a direct role of NAC in mitochondrial targeting cannot be excluded, our data suggest that mitochondrial defects upon NAC depletion[16,41–43,45,64] may arise from impaired co-translational chaperoning of folding domains, MTSs, or TMDs, rather than direct disruption of import machineries. In agreement, NAC depletion was shown to not affect the translocase of the outer mitochondrial membrane (TOM)-dependent import.[48]

In conclusion, NAC acts as a general coordinator of ribosome and nascent chain accessibility while serving as a broad co-translational chaperone. These findings provide an insight into NAC's multifaceted role in protein biogenesis.

Limitations of the study

Immunoprecipitation-based approaches, including SeRP, may capture interactions mediated by a third component. Thus, some identified binding periods could theoretically involve an additional protein crosslinked to both NAC and the nascent chain. However, the low efficiency of crosslinking reactions makes the likelihood of two simultaneous linkages occurring within the same complex orders of magnitude lower than direct crosslinking. Consistently, smFRET, cryo-EM, and optical tweezer experiments performed in reconstituted *in vitro* systems

support that the NAC binding periods observed by SeRP represent direct interactions with nascent chains.

Crosslinking-based approaches, like the one used here, may miss interactions lacking crosslinkable residues. However, lysines are abundant (~5%–7% of residues in human proteins), and the N-terminal amino group of nascent chains is also crosslinkable. Thus, while a small fraction of interactions may escape detection, this is a trade-off inherent to translatome-wide approaches, provided it does not bias the conclusions, as addressed in Figure S1.

Surprisingly, we did not observe major physicochemical differences between NAC-bound and non-bound SP and TMDs, indicating that NAC binding is not dictated by sequence alone. Factors like localized translation at the ER, translation kinetics, and competition (or cooperation) with other factors may influence these interactions. Importantly, SeRP captures interactions that persist over multiple codons, so short-lived interactions outcompeted within 1–3 codons may be underrepresented. Thus, our data hint at different pathways and variable NAC dependencies or binding dynamics for SP- and TMD-driven co-translational translocation, which could be explored in future studies.

RESOURCE AVAILABILITY

Lead contact

Further information and requests for resources and reagents should be directed to and will be fulfilled by the lead contact, Bernd Bukau (bukau@zmbh.uni-heidelberg.de).

Materials availability

All unique/stable reagents generated in this study are available from the lead contact with a completed material transfer agreement.

Data and code availability

- All sequencing data reported in this study are available at GEO under accession number GSE: 290865 and are publicly available as of the date of publication. Models and electron microscopy maps were deposited at the PDB and EMDB with accession codes–PDB: 28LN and EMDB: EMD-56598, EMD-56582, and EMD-56583 and are publicly available as of the date of publication.
- Binding period determination was performed using in-house Python scripts (available at https://github.com/JaimeSantos-BukauLab/Santos-et-al.-2025; DOI: 10.5281/zenodo.18552680). Additional analysis for the ribosome profiling dataset was conducted using RiboSeqTools (available at https://github.com/ilia-kats/RiboSeqTools).
- Any additional information required to reanalyze the data reported in this paper is available from the lead contact upon request.

ACKNOWLEDGMENTS

B.B., S.J.T., and N.B. acknowledge support from the European Research Council (ERC SyG CoTransComplex, grant 101072047). The views and opinions expressed are those of the authors only and do not necessarily reflect those of the European Union or the European Research Council. Neither the European Union nor the granting authority can be held responsible for them. B.B. and G.K. were supported by the Deutsche Forschungsgemeinschaft (DFG; KR3593/4-1); S.-o.S. and R.J.G. by NIH grant R35/GM136321 and NSF grant 2219287; N.B. by the Swiss National Science Foundation (SNSF 310030_212308); J.S. by an EMBO postdoctoral fellowship; and M.P. by a Boehringer Ingelheim Fonds PhD fellowship. We thank B. Echeverria Perez for preparation of the NAC construct for single-molecule experiments and A. Scaiola, M. Leibundgut, and T. Schönhut for assistance with cryo-EM data collection, model building, and purification of the NAC mutant.

AUTHOR CONTRIBUTIONS

Conceptualization, J.S., M.G., R.J.G., M.I., M.P., N.B., S.J.T., S.-o.S., G.K., and B.B. Methodology, J.S., M.G., R.J.G., M.I., M.P., I.E.K., N.B., S.J.T., S.-o.S., G.K., and B.B. Investigation, J.S., M.G., R.J.G., M.I., M.P., I.E.K., P.D., D.C., and J.J. Software, J.S., M.G., and F.T. Formal analysis, data curation, and visualization, J.S., M.G., R.J.G., M.I., M.P., I.E.K., C.H., N.B., S.J.T., S.-o.S., G.K., and B.B. Writing—original draft, J.S., G.K., and B.B. Writing—review & editing, all authors. Supervision and funding acquisition, N.B., S.J.T., S.-o.S., G.K., and B.B.

DECLARATION OF INTERESTS

The authors declare no competing interests.

DECLARATION OF GENERATIVE AI AND AI-ASSISTED TECHNOLOGIES IN THE WRITING PROCESS

During the preparation of this work, the authors used ChatGPT in order to improve language and readability. After using this tool, the authors reviewed and edited the content as needed and take full responsibility for the content of the publication.

STAR★METHODS

Detailed methods are provided in the online version of this paper and include the following:

- KEY RESOURCES TABLE
- EXPERIMENTAL MODEL AND STUDY PARTICIPANT DETAILS
  - Cell culture
- METHOD DETAILS
  - Selective ribosome profiling
  - Bioinformatic analysis
  - Protein Preparation for smTIRF microscopy
  - RNC_{hRPL4} Purification
  - Single-molecule TIRF microscopy
  - Single-molecule FRET data analysis
  - Cryo-EM sample preparation
  - Cryo-EM methods
  - Single-molecule optical tweezers
- QUANTIFICATION AND STATISTICAL ANALYSIS

SUPPLEMENTAL INFORMATION

Supplemental information can be found online at https://doi.org/10.1016/j.molcel.2026.02.022.

Received: April 3, 2025
Revised: December 10, 2025
Accepted: February 24, 2026
Published: March 23, 2026

REFERENCES

1. Cassaignau, A.M.E., Cabrita, L.D., and Christodoulou, J. (2020). How Does the Ribosome Fold the Proteome? Annu. Rev. Biochem. *89*, 389–415. https://doi.org/10.1146/annurev-biochem-062917-012226.
2. Gamerdinger, M., Jia, M., Schloemer, R., Rabl, L., Jaskolowski, M., Khakzar, K.M., Ulusoy, Z., Wallisch, A., Jomaa, A., Hunaeus, G., et al. (2023). NAC controls cotranslational N-terminal methionine excision in

eukaryotes. Science *380*, 1238–1243. https://doi.org/10.1126/science.adg3297.

3. Jomaa, A., Gamerdinger, M., Hsieh, H.-H., Wallisch, A., Chandrasekaran, V., Ulusoy, Z., Scaiola, A., Hegde, R.S., Shan, S.-O., Ban, N., et al. (2022). Mechanism of signal sequence handover from NAC to SRP on ribosomes during ER-protein targeting. Science *375*, 839–844. https://doi.org/10.1126/science.abl6459.
4. Lentzsch, A.M., Yudin, D., Gamerdinger, M., Chandrasekar, S., Rabl, L., Scaiola, A., Deuerling, E., Ban, N., and Shan, S.-O. (2024). NAC guides a ribosomal multienzyme complex for nascent protein processing. Nature *633*, 718–724. https://doi.org/10.1038/s41586-024-07846-7.
5. Gilmore, R., Blobel, G., and Walter, P. (1982). Protein translocation across the endoplasmic reticulum. I. Detection in the microsomal membrane of a receptor for the signal recognition particle. J. Cell Biol. *95*, 463–469. https://doi.org/10.1083/jcb.95.2.463.
6. Halic, M., Blau, M., Becker, T., Mielke, T., Pool, M.R., Wild, K., Sinning, I., and Beckmann, R. (2006). Following the signal sequence from ribosomal tunnel exit to signal recognition particle. Nature *444*, 507–511. https://doi.org/10.1038/nature05326.
7. Streit, J.O., Bukvin, I.V., Chan, S.H.S., Bashir, S., Woodburn, L.F., Włodarski, T., Figueiredo, A.M., Jurkeviciute, G., Sidhu, H.K., Hornby, C.R., et al. (2024). The ribosome lowers the entropic penalty of protein folding. Nature *633*, 232–239. https://doi.org/10.1038/s41586-024-07784-4.
8. Bertolini, M., Fenzl, K., Kats, I., Wruck, F., Tippmann, F., Schmitt, J., Auburger, J.J., Tans, S., Bukau, B., and Kramer, G. (2021). Interactions between nascent proteins translated by adjacent ribosomes drive homomer assembly. Science *371*, 57–64. https://doi.org/10.1126/science.abc7151.
9. Shiber, A., Döring, K., Friedrich, U., Klann, K., Merker, D., Zedan, M., Tippmann, F., Kramer, G., and Bukau, B. (2018). Cotranslational assembly of protein complexes in eukaryotes revealed by ribosome profiling. Nature *561*, 268–272. https://doi.org/10.1038/s41586-018-0462-y.
10. Shieh, Y.-W., Minguez, P., Bork, P., Auburger, J.J., Guilbride, D.L., Kramer, G., and Bukau, B. (2015). Operon structure and cotranslational subunit association direct protein assembly in bacteria. Science *350*, 678–680. https://doi.org/10.1126/science.aac8171.
11. Gamerdinger, M., Kobayashi, K., Wallisch, A., Kreft, S.G., Sailer, C., Schlömer, R., Sachs, N., Jomaa, A., Stengel, F., Ban, N., et al. (2019). Early Scanning of Nascent Polypeptides inside the Ribosomal Tunnel by NAC. Mol. Cell *75*, 996–1006.e8. https://doi.org/10.1016/j.molcel.2019.06.030.
12. Wiedmann, B., Sakai, H., Davis, T.A., and Wiedmann, M. (1994). A protein complex required for signal-sequence-specific sorting and translocation. Nature *370*, 434–440. https://doi.org/10.1038/370434a0.
13. Klein, M., Wild, K., and Sinning, I. (2024). Multi-protein assemblies orchestrate co-translational enzymatic processing on the human ribosome. Nat. Commun. *15*, 7681. https://doi.org/10.1038/s41467-024-51964-9.
14. Minoia, M., Quintana-Cordero, J., Jetzinger, K., Kotan, I.E., Turnbull, K.J., Ciccarelli, M., Masser, A.E., Liebers, D., Gouarin, E., Czech, M., et al. (2024). Chp1 is a dedicated chaperone at the ribosome that safeguards eEF1A biogenesis. Chp1. Nat. Commun. *15*, 1382. https://doi.org/10.1038/s41467-024-45645-w.
15. Gamerdinger, M., Hanebuth, M.A., Frickey, T., and Deuerling, E. (2015). The principle of antagonism ensures protein targeting specificity at the endoplasmic reticulum. Science *348*, 201–207. https://doi.org/10.1126/science.aaa5335.
16. Fünfschilling, U., and Rospert, S. (1999). Nascent polypeptide-associated complex stimulates protein import into yeast mitochondria. Mol. Biol. Cell *10*, 3289–3299. https://doi.org/10.1091/mbc.10.10.3289.
17. Raue, U., Oellerer, S., and Rospert, S. (2007). Association of protein biogenesis factors at the yeast ribosomal tunnel exit is affected by the translational status and nascent polypeptide sequence. J. Biol. Chem. *282*, 7809–7816. https://doi.org/10.1074/jbc.M611436200.
18. Wegrzyn, R.D., Hofmann, D., Merz, F., Nikolay, R., Rauch, T., Graf, C., and Deuerling, E. (2006). A conserved motif is prerequisite for the interaction of NAC with ribosomal protein L23 and nascent chains. J. Biol. Chem. *281*, 2847–2857. https://doi.org/10.1074/jbc.M511420200.
19. Jumper, J., Evans, R., Pritzel, A., Green, T., Figurnov, M., Ronneberger, O., Tunyasuvunakool, K., Bates, R., Žídek, A., Potapenko, A., et al. (2021). Highly accurate protein structure prediction with AlphaFold. Nature *596*, 583–589. https://doi.org/10.1038/s41586-021-03819-2.
20. Varadi, M., Bertoni, D., Magana, P., Paramval, U., Pidruchna, I., Radhakrishnan, M., Tsenkov, M., Nair, S., Mirdita, M., Yeo, J., et al. (2024). AlphaFold Protein Structure Database in 2024: providing structure coverage for over 214 million protein sequences. Nucleic Acids Res. *52*, D368–D375. https://doi.org/10.1093/nar/gkad1011.
21. Deuerling, E., Gamerdinger, M., and Kreft, S.G. (2019). Chaperone Interactions at the Ribosome. Cold Spring Harb. Perspect. Biol. *11*, a033977. https://doi.org/10.1101/cshperspect.a033977.
22. Wang, F., Durfee, L.A., and Huibregtse, J.M. (2013). A cotranslational ubiquitination pathway for quality control of misfolded proteins. Mol. Cell *50*, 368–378. https://doi.org/10.1016/j.molcel.2013.03.009.
23. Duttler, S., Pechmann, S., and Frydman, J. (2013). Principles of cotranslational ubiquitination and quality control at the ribosome. Mol. Cell *50*, 379–393. https://doi.org/10.1016/j.molcel.2013.03.010.
24. Deuerling, E., and Bukau, B. (2004). Chaperone-assisted folding of newly synthesized proteins in the cytosol. Crit. Rev. Biochem. Mol. Biol. *39*, 261–277. https://doi.org/10.1080/10409230490892496.
25. Preissler, S., and Deuerling, E. (2012). Ribosome-associated chaperones as key players in proteostasis. Trends Biochem. Sci. *37*, 274–283. https://doi.org/10.1016/j.tibs.2012.03.002.
26. Kirstein-Miles, J., Scior, A., Deuerling, E., and Morimoto, R.I. (2013). The nascent polypeptide-associated complex is a key regulator of proteostasis. EMBO J. *32*, 1451–1468. https://doi.org/10.1038/emboj.2013.87.
27. Shen, K., Gamerdinger, M., Chan, R., Gense, K., Martin, E.M., Sachs, N., Knight, P.D., Schlömer, R., Calabrese, A.N., Stewart, K.L., et al. (2019). Dual Role of Ribosome-Binding Domain of NAC as a Potent Suppressor of Protein Aggregation and Aging-Related Proteinopathies. Mol. Cell *74*, 729–741.e7. https://doi.org/10.1016/j.molcel.2019.03.012.
28. Martin, E.M., Jackson, M.P., Gamerdinger, M., Gense, K., Karamonos, T.K., Humes, J.R., Deuerling, E., Ashcroft, A.E., and Radford, S.E. (2018). Conformational flexibility within the nascent polypeptide-associated complex enables its interactions with structurally diverse client proteins. J. Biol. Chem. *293*, 8554–8568. https://doi.org/10.1074/jbc.RA117.001568.
29. Koplin, A., Preissler, S., Ilina, Y., Koch, M., Scior, A., Erhardt, M., and Deuerling, E. (2010). A dual function for chaperones SSB-RAC and the NAC nascent polypeptide-associated complex on ribosomes. J. Cell Biol. *189*, 57–68. https://doi.org/10.1083/jcb.200910074.
30. Zhu, Z., Wang, S., and Shan, S.-O. (2022). Ribosome profiling reveals multiple roles of SecA in cotranslational protein export. Nat. Commun. *13*, 3393. https://doi.org/10.1038/s41467-022-31061-5.
31. Stein, K.C., Kriel, A., and Frydman, J. (2019). Nascent Polypeptide Domain Topology and Elongation Rate Direct the Cotranslational Hierarchy of Hsp70 and TRiC/CCT. Mol. Cell *75*, 1117–1130.e5. https://doi.org/10.1016/j.molcel.2019.06.036.
32. Galmozzi, C.V., Merker, D., Friedrich, U.A., Döring, K., and Kramer, G. (2019). Selective ribosome profiling to study interactions of translating ribosomes in yeast. Nat. Protoc. *14*, 2279–2317. https://doi.org/10.1038/s41596-019-0185-z.
33. Döring, K., Ahmed, N., Riemer, T., Suresh, H.G., Vainshtein, Y., Habich, M., Riemer, J., Mayer, M.P., O'Brien, E.P., Kramer, G., et al. (2017). Profiling Ssb-Nascent Chain Interactions Reveals Principles of Hsp70-Assisted Folding. Cell *170*, 298–311.e20. https://doi.org/10.1016/j.cell.2017.06.038.

34. Chartron, J.W., Hunt, K.C.L., and Frydman, J. (2016). Cotranslational signal-independent SRP preloading during membrane targeting. Nature *536*, 224–228. https://doi.org/10.1038/nature19309.

35. Schibich, D., Gloge, F., Pöhner, I., Björkholm, P., Wade, R.C., von Heijne, G., Bukau, B., and Kramer, G. (2016). Global profiling of SRP interaction with nascent polypeptides. Nature *536*, 219–223. https://doi.org/10.1038/nature19070.

36. Oh, E., Becker, A.H., Sandikci, A., Huber, D., Chaba, R., Gloge, F., Nichols, R.J., Typas, A., Gross, C.A., Kramer, G., et al. (2011). Selective ribosome profiling reveals the cotranslational chaperone action of trigger factor in vivo. Cell *147*, 1295–1308. https://doi.org/10.1016/j.cell.2011.10.044.

37. Ingolia, N.T., Ghaemmaghami, S., Newman, J.R.S., and Weissman, J.S. (2009). Genome-wide analysis in vivo of translation with nucleotide resolution using ribosome profiling. Science *324*, 218–223. https://doi.org/10.1126/science.1168978.

38. Hsieh, H.-H., Lee, J.H., Chandrasekar, S., and Shan, S.-O. (2020). A ribosome-associated chaperone enables substrate triage in a cotranslational protein targeting complex. Nat. Commun. *11*, 5840. https://doi.org/10.1038/s41467-020-19548-5.

39. del Alamo, M., Hogan, D.J., Pechmann, S., Albanese, V., Brown, P.O., and Frydman, J. (2011). Defining the specificity of cotranslationally acting chaperones by systematic analysis of mRNAs associated with ribosome-nascent chain complexes. PLoS Biol. *9*, e1001100. https://doi.org/10.1371/journal.pbio.1001100.

40. Becker, A.H., Oh, E., Weissman, J.S., Kramer, G., and Bukau, B. (2013). Selective ribosome profiling as a tool for studying the interaction of chaperones and targeting factors with nascent polypeptide chains and ribosomes. Nat. Protoc. *8*, 2212–2239. https://doi.org/10.1038/nprot.2013.133.

41. Ponce-Rojas, J.C., Avendaño-Monsalve, M.C., Yañez-Falcón, A.R., Jaimes-Miranda, F., Garay, E., Torres-Quiroz, F., DeLuna, A., and Funes, S. (2017). αβ'-NAC cooperates with Sam37 to mediate early stages of mitochondrial protein import. FEBS Journal *284*, 814–830. https://doi.org/10.1111/febs.14024.

42. Lesnik, C., Cohen, Y., Atir-Lande, A., Schuldiner, M., and Arava, Y. (2014). OM14 is a mitochondrial receptor for cytosolic ribosomes that supports co-translational import into mitochondria. Nat. Commun. *5*, 5711. https://doi.org/10.1038/ncomms6711.

43. George, R., Beddoe, T., Landl, K., and Lithgow, T. (1998). The yeast nascent polypeptide-associated complex initiates protein targeting to mitochondria in vivo. Proc. Natl. Acad. Sci. USA *95*, 2296–2301. https://doi.org/10.1073/pnas.95.5.2296.

44. Wiedemann, N., and Pfanner, N. (2017). Mitochondrial Machineries for Protein Import and Assembly. Annu. Rev. Biochem. *86*, 685–714. https://doi.org/10.1146/annurev-biochem-060815-014352.

45. Muthukumar, G., Stevens, T.A., Inglis, A.J., Esantsi, T.K., Saunders, R.A., Schulte, F., Voorhees, R.M., Guna, A., and Weissman, J.S. (2024). Triaging of α-helical proteins to the mitochondrial outer membrane by distinct chaperone machinery based on substrate topology. Mol. Cell *84*, 1101–1119.e9. https://doi.org/10.1016/j.molcel.2024.01.028.

46. Kyte, J., and Doolittle, R.F. (1982). A simple method for displaying the hydropathic character of a protein. J. Mol. Biol. *157*, 105–132. https://doi.org/10.1016/0022-2836(82)90515-0.

47. Eisenberg, D., Weiss, R.M., and Terwilliger, T.C. (1982). The helical hydrophobic moment: a measure of the amphiphilicity of a helix. Nature *299*, 371–374. https://doi.org/10.1038/299371a0.

48. Zhu, Z., Mallik, S., Stevens, T.A., Huang, R., Levy, E.D., and Shan, S.-O. (2025). Principles of cotranslational mitochondrial protein import. Cell *188*, 5605–5617.e14. https://doi.org/10.1016/j.cell.2025.07.021.

49. Zhang, Z., and Presgraves, D.C. (2017). Translational compensation of gene copy number alterations by aneuploidy in Drosophila melanogaster. Nucleic Acids Res. *45*, 2986–2993. https://doi.org/10.1093/nar/gkx106.

50. Senger, G., Santaguida, S., and Schaefer, M.H. (2022). Regulation of protein complex partners as a compensatory mechanism in aneuploid tumors. eLife *11*, e75526. https://doi.org/10.7554/eLife.75526.

51. Schneider, K., Nelson, G.M., Watson, J.L., Morf, J., Dalglish, M., Luh, L.M., Weber, A., and Bertolotti, A. (2020). Protein Stability Buffers the Cost of Translation Attenuation following eIF2α Phosphorylation. Cell Rep. *32*, 108154. https://doi.org/10.1016/j.celrep.2020.108154.

52. Pillet, B., García-Gómez, J.J., Pausch, P., Falquet, L., Bange, G., de la Cruz, J., and Kressler, D. (2015). The Dedicated Chaperone Acl4 Escorts Ribosomal Protein Rpl4 to Its Nuclear Pre-60S Assembly Site. PLoS Genet. *11*, e1005565. https://doi.org/10.1371/journal.pgen.1005565.

53. Lin, Z., Gasic, I., Chandrasekaran, V., Peters, N., Shao, S., Mitchison, T.J., and Hegde, R.S. (2020). TTC5 mediates autoregulation of tubulin via mRNA degradation. Science *367*, 100–104. https://doi.org/10.1126/science.aaz4352.

54. Avellaneda, M.J., Koers, E.J., Minde, D.P., Sunderlikova, V., and Tans, S.J. (2020). Simultaneous sensing and imaging of individual biomolecular complexes enabled by modular DNA-protein coupling. Commun. Chem. *3*, 20. https://doi.org/10.1038/s42004-020-0267-4.

55. Mashaghi, A., Kramer, G., Bechtluft, P., Zachmann-Brand, B., Driessen, A.J.M., Bukau, B., and Tans, S.J. (2013). Reshaping of the conformational search of a protein by the chaperone trigger factor. Nature *500*, 98–101. https://doi.org/10.1038/nature12293.

56. Mashaghi, A., Bezrukavnikov, S., Minde, D.P., Wentink, A.S., Kityk, R., Zachmann-Brand, B., Mayer, M.P., Kramer, G., Bukau, B., and Tans, S.J. (2016). Alternative modes of client binding enable functional plasticity of Hsp70. Nature *539*, 448–451. https://doi.org/10.1038/nature20137.

57. Naqvi, M.M., Avellaneda, M.J., Roth, A., Koers, E.J., Roland, A., Sunderlikova, V., Kramer, G., Rye, H.S., and Tans, S.J. (2022). Protein chain collapse modulation and folding stimulation by GroEL-ES. Sci. Adv. *8*, eabl6293. https://doi.org/10.1126/sciadv.abl6293.

58. Bechtluft, P., van Leeuwen, R.G.H., Tyreman, M., Tomkiewicz, D., Nouwen, N., Tepper, H.L., Driessen, A.J.M., and Tans, S.J. (2007). Direct observation of chaperone-induced changes in a protein folding pathway. Science *318*, 1458–1461. https://doi.org/10.1126/science.1144972.

59. Dobson, C.M. (2003). Protein folding and misfolding. Nature *426*, 884–890. https://doi.org/10.1038/nature02261.

60. Sharma, S., Chakraborty, K., Müller, B.K., Astola, N., Tang, Y.-C., Lamb, D.C., Hayer-Hartl, M., and Hartl, F.U. (2008). Monitoring protein conformation along the pathway of chaperonin-assisted folding. Cell *133*, 142–153. https://doi.org/10.1016/j.cell.2008.01.048.

61. Mogk, A., Ruger-Herreros, C., and Bukau, B. (2019). Cellular Functions and Mechanisms of Action of Small Heat Shock Proteins. Annu. Rev. Microbiol. *73*, 89–110. https://doi.org/10.1146/annurev-micro-020518-115515.

62. Karagöz, G.E., and Rüdiger, S.G.D. (2015). Hsp90 interaction with clients. Trends Biochem. Sci. *40*, 117–125. https://doi.org/10.1016/j.tibs.2014.12.002.

63. Juszkiewicz, S., Peak-Chew, S.-Y., and Hegde, R.S. (2025). Mechanism of chaperone recruitment and retention on mitochondrial precursors. Mol. Biol. Cell *36*, ar39. https://doi.org/10.1091/mbc.E25-01-0035.

64. Ramalho, S., Alkan, F., Prekovic, S., Jastrzebski, K., Barberà, E.P., Hoekman, L., Altelaar, M., de Heus, C., Liv, N., Rodríguez-Colman, M.J., et al. (2025). NAC regulates metabolism and cell fate in intestinal stem cells. Sci. Adv. *11*, eadn9750. https://doi.org/10.1126/sciadv.adn9750.

65. Bothe, A., and Ban, N. (2024). A highly optimized human in vitro translation system. Cell Rep. Methods *4*, 100755. https://doi.org/10.1016/j.crmeth.2024.100755.

66. Huang, D.W., Sherman, B.T., and Lempicki, R.A. (2009). Systematic and integrative analysis of large gene lists using DAVID bioinformatics resources. Nat. Protoc. *4*, 44–57. https://doi.org/10.1038/nprot.2008.211.

67. Mészáros, B., Erdos, G., and Dosztányi, Z. (2018). IUPred2A: context-dependent prediction of protein disorder as a function of redox state

and protein binding. Nucleic Acids Res. *46*, W329–W337. https://doi.org/10.1093/nar/gky384.

68. Vacic, V., Iakoucheva, L.M., and Radivojac, P. (2006). Two Sample Logo: a graphical representation of the differences between two sets of sequence alignments. Bioinformatics *22*, 1536–1537. https://doi.org/10.1093/bioinformatics/btl151.
69. Preus, S., Noer, S.L., Hildebrandt, L.L., Gudnason, D., and Birkedal, V. (2015). iSMS: single-molecule FRET microscopy software. Nat. Methods *12*, 593–594. https://doi.org/10.1038/nmeth.3435.
70. Delgado, J., Reche, R., Cianferoni, D., Orlando, G., van der Kant, R., Rousseau, F., Schymkowitz, J., and Serrano, L. (2025). FoldX force field revisited, an improved version. Bioinformatics *41*, btaf064. https://doi.org/10.1093/bioinformatics/btaf064.
71. Punjani, A., Rubinstein, J.L., Fleet, D.J., and Brubaker, M.A. (2017). cryoSPARC: algorithms for rapid unsupervised cryo-EM structure determination. Nat. Methods *14*, 290–296. https://doi.org/10.1038/nmeth.4169.
72. Pettersen, E.F., Goddard, T.D., Huang, C.C., Meng, E.C., Couch, G.S., Croll, T.I., Morris, J.H., and Ferrin, T.E. (2021). UCSF ChimeraX: Structure visualization for researchers, educators, and developers. Protein Sci. *30*, 70–82. https://doi.org/10.1002/pro.3943.
73. Emsley, P., Lohkamp, B., Scott, W.G., and Cowtan, K. (2010). Features and development of Coot. Acta Crystallogr., D *66*, 486–501. https://doi.org/10.1107/S0907444910007493.
74. Liebschner, D., Afonine, P.V., Baker, M.L., Bunkóczi, G., Chen, V.B., Croll, T.I., Hintze, B., Hung, L.W., Jain, S., McCoy, A.J., et al. (2019). Macromolecular structure determination using X-rays, neutrons and electrons: recent developments in Phenix. Acta Crystallogr. D Struct. Biol. *75*, 861–877. https://doi.org/10.1107/S2059798319011471.
75. Günnigmann, M., Koubek, J., Kramer, G., and Bukau, B. (2023). Selective ribosome profiling as a tool to study interactions of translating ribosomes in mammalian cells. Methods Enzymol. *684*, 1–38. https://doi.org/10.1016/bs.mie.2022.09.006.
76. McGlincy, N.J., and Ingolia, N.T. (2017). Transcriptome-wide measurement of translation by ribosome profiling. Methods *126*, 112–129. https://doi.org/10.1016/j.ymeth.2017.05.028.
77. Koubek, J., Jetzinger, K., Dror, S., Irastortza-Olaziregi, M., Frank, D., Kotan, I., Santos, J., Tippmann, F., Lafrenz, P., Kaessmann, H., et al. (2025). A simple, fast, and cost-efficient protocol for ultra-sensitive ribosome profiling. Nucleic Acids Res. *53*, gkaf902. https://doi.org/10.1093/nar/gkaf902.
78. Manriquez-Sandoval, E., and Fried, S.D. (2022). DomainMapper: Accurate domain structure annotation including those with non-contiguous topologies. Protein Sci. *31*, e4465. https://doi.org/10.1002/pro.4465.
79. UniProt Consortium (2019). UniProt: a worldwide hub of protein knowledge. Nucleic Acids Res. *47*, D506–D515. https://doi.org/10.1093/nar/gky1049.
80. Rath, S., Sharma, R., Gupta, R., Ast, T., Chan, C., Durham, T.J., Goodman, R.P., Grabarek, Z., Haas, M.E., Hung, W.H.W., et al. (2021). MitoCarta3.0: an updated mitochondrial proteome now with sub-organelle localization and pathway annotations. Nucleic Acids Res. *49*, D1541–D1547. https://doi.org/10.1093/nar/gkaa1011.
81. Sprenger, J., Lynn Fink, J., Karunaratne, S., Hanson, K., Hamilton, N.A., and Teasdale, R.D. (2008). LOCATE: a mammalian protein subcellular localization database. Nucleic Acids Res. *36*, D230–D233. https://doi.org/10.1093/nar/gkm950.
82. Ashburner, M., Ball, C.A., Blake, J.A., Botstein, D., Butler, H., Cherry, J.M., Davis, A.P., Dolinski, K., Dwight, S.S., Eppig, J.T., et al. (2000). Gene ontology: tool for the unification of biology. The Gene Ontology Consortium. Nat. Genet. *25*, 25–29. https://doi.org/10.1038/75556.
83. Aitken, C.E., Marshall, R.A., and Puglisi, J.D. (2008). An oxygen scavenging system for improvement of dye stability in single-molecule fluorescence experiments. Biophys. J. *94*, 1826–1835. https://doi.org/10.1529/biophysj.107.117689.
84. Shen, K., Arslan, S., Akopian, D., Ha, T., and Shan, S.O. (2012). Activated GTPase movement on an RNA scaffold drives co-translational protein targeting. Nature *492*, 271–275. https://doi.org/10.1038/nature11726.
85. van de Meent, J.-W., Bronson, J.E., Wiggins, C.H., and Gonzalez, R.L. (2014). Empirical Bayes Methods Enable Advanced Population-Level Analyses of Single-Molecule FRET Experiments. Biophys. J. *106*, 1327–1337. https://doi.org/10.1016/j.bpj.2013.12.055.
86. Shanmuganathan, V., Schiller, N., Magoulopoulou, A., Cheng, J., Braunger, K., Cymer, F., Berninghausen, O., Beatrix, B., Kohno, K., von Heijne, G., et al. (2019). Structural and mutational analysis of the ribosome-arresting human XBP1u. eLife *8*, e46267. https://doi.org/10.7554/eLife.46267.
87. Yariv, B., Yariv, E., Kessel, A., Masrati, G., Chorin, A.B., Martz, E., Mayrose, I., Pupko, T., and Ben-Tal, N. (2023). Using evolutionary data to make sense of macromolecules with a "face-lifted" ConSurf. Protein Sci. *32*, e4582. https://doi.org/10.1002/pro.4582.
88. Stevens, T.A., Tomaleri, G.P., Hazu, M., Wei, S., Nguyen, V.N., DeKalb, C., Voorhees, R.M., and Pleiner, T. (2024). A nanobody-based strategy for rapid and scalable purification of human protein complexes. Nat. Protoc. *19*, 127–158. https://doi.org/10.1038/s41596-023-00904-w.
89. Chan, P.P., and Lowe, T.M. (2016). GtRNAdb 2.0: an expanded database of transfer RNA genes identified in complete and draft genomes. Nucleic Acids Res. *44*, D184–D189. https://doi.org/10.1093/nar/gkv1309.
90. Schüttelkopf, A.W., and van Aalten, D.M.F. (2004). PRODRG: a tool for high-throughput crystallography of protein-ligand complexes. Acta Crystallogr., D *60*, 1355–1363. https://doi.org/10.1107/S0907444904011679.
91. Chen, V.B., Arendall, W.B., Headd, J.J., Keedy, D.A., Immormino, R.M., Kapral, G.J., Murray, L.W., Richardson, J.S., and Richardson, D.C. (2010). MolProbity: all-atom structure validation for macromolecular crystallography. Acta Crystallogr., D *66*, 12–21. https://doi.org/10.1107/S0907444909042073.
92. Dudko, O.K., Hummer, G., and Szabo, A. (2008). Theory, analysis, and interpretation of single-molecule force spectroscopy experiments. Proc. Natl. Acad. Sci. USA *105*, 15755–15760. https://doi.org/10.1073/pnas.0806085105.

STAR★METHODS

KEY RESOURCES TABLE

REAGENT or RESOURCE	SOURCE	IDENTIFIER
Antibodies		
NACβ antibody, rabbit polyclonal	Homemade	N/A
NACα antibody, rabbit polyclonal	Homemade	N/A
Rps6 (C-8, Santa Cruz; cat. no. sc-74459	Santa Cruz	Cat# sc-74459; RRID:AB_1129205
Polyclonal GFP primary antibody	Invitrogen	Cat# A6455; RRID:AB_221570
Bacterial and virus strains		
E. coli BL21 (DE3) cells	Merck	Cat# 69450-3
Chemicals, peptides, and recombinant proteins		
RNase I (Ambion)	Invitrogen	Cat# AM2294
Pierce Premium Grade DSP	Thermo Scientific	Cat# PG82081
SUPERase·In RNase Inhibitor	Invitrogen	Cat# AM2696
Indole-3-acetic acid sodium	Santa Cruz	Cat# sc-215171
5′-Biotin-G-Monophosphate	TriLink Biotechnologies	Cat# N-6003
VECTABOND Reagent	Vector Laboratories	Cat #SP-1800-7
NeutrAvidin Protein	ThermoFisher Scientific	Cat# 31000
Trolox	Millipore Sigma	Cat #648471
3,4-Dihydroxybenzoic acid, 97% (PCA)	ThermoFisher Scientific	Cat #114895000
Protocatechuate-3,4-dioxygenase (PCD)	Millipore Sigma	Cat #P8279
Cycloheximide	Sigma	Cat# C1988-1G
Human NACα-NACβ	This study	N/A
Human NACα (I128N)-NACβ (V53S, L83N)	This study	N/A
Critical commercial assays		
Qubit Broad Range RNA assay	Invitrogen	Cat# Q10211
NEXTflex Small RNA-Seq Kit v3	PerkinElmer	Cat# 5132-06
Deposited data		
Raw sequencing data	This paper	GEO: GSE290865
Atomic model of XBP1u-stalled RPL4 RNC in complex with NAC	This paper	PDB: 28LN
Cryo-EM density map of XBP1u-stalled RPL4 RNC in complex with NAC	This paper	EMDB: EMD-56598
Cryo-EM density map of XBP1u-stalled RPL4 RNC in complex with NAC (locally refined on 40S body)	This paper	EMDB: EMD-56582
Cryo-EM density map of XBP1u-stalled RPL4 RNC in complex with NAC (locally refined on 40S head)	This paper	EMDB: EMD-56583
Experimental models: Cell lines		
HEK293-T cells	DSMZ	Cat# ACC 635
NACβ-AID cell line	Zhu et al.[48]	N/A
Oligonucleotides		
PCR oligonucleotides used to linearize RPL4 plasmid 5′-GTGCTGCAAGGCGATTAAG-3′ (forward) 5′-GAAGCCCGGATATAGTTCC-3′ (reverse)	Microsynth	N/A

(*Continued on next page*)

Continued

REAGENT or RESOURCE	SOURCE	IDENTIFIER
Recombinant DNA		
pET28b-6×His-NACα-NACβ (S57C mutation for labeling)	Hsieh et al.[38]	N/A
pT7CFE1-CHis	Thermo Fischer Scientific	Cat# 88860
pT7CFE1-EGFP-SUMO-RPL4(1-158 aa)-XBP1u	This study	N/A
pRSET-A-His6-GADD34Δ1-240	Bothe and Ban[65]	N/A
p6xHis-TEV-NACα-NACβ	This study	N/A
p6xHis-TEV-NACα(I128N)-NACβ(V53S, L83N)	This study	N/A
Software and algorithms		
DAVID Bioinformatics Resources	Huang et al.[66]	https://davidbioinformatics.nih.gov/
Binding period determination scripts	This paper	https://github.com/JaimeSantos-BukauLab/Santos-et-al.-2025; DOI: 10.5281/zenodo.18552680].
Human Alphafold derived structures	Jumper et al.[19] and Varadi et al.[20]	https://alphafold.ebi.ac.uk/download
RiboSeqTools	Bukau lab	https://github.com/ilia-kats/RiboSeqTools
IUPRED 2.0	Mészáros et al.[67]	https://iupred2a.elte.hu/
Two Sample Logo	Vacic et al.[68]	https://www.twosamplelogo.org/
iSMS software	Preus et al.[69]	https://inano.au.dk/about/research-groups/single-molecule-biophysics-and-chemistry-group/software
FoldX	Delgado et al.[70]	https://foldxsuite.crg.eu/
CryoSPARC	Punjani et al.[71]	https://cryosparc.com/
UCSF ChimeraX	Pettersen et al.[72]	https://www.cgl.ucsf.edu/chimerax/
COOT	Emsley et al.[73]	https://www2.mrc-lmb.cam.ac.uk/personal/pemsley/coot/
PHENIX	Liebschner et al.[74]	https://www.phenix-online.org/
Other		
Protein A Dynabeads	ThermoFisher	Cat# 10002D
anti-DYKDDDK magnetic agarose beads	Pierce	Cat# A36797
Rabbit reticulocyte lysate (RRL)	Green Hectares	N/A
Neutravidin-coated polystyrene beads (2.08 μm)	Spherotech	Cat# NVP-20-5
HeLa cytoplasmic extract	IPRACELL	Cat# CC-01-40-50
Pierce streptavidin magnetic beads (for GFP nanobody conjugation)	Thermo Scientific	Cat# 88816
Anti-digoxigenin antibody-coated polystyrene beads (2.11 μm)	Spherotech	Cat# DIGP-20-2

EXPERIMENTAL MODEL AND STUDY PARTICIPANT DETAILS

Cell culture

HEK293-T cells (Homo sapiens embryonal kidney, DSMZ Cat# ACC 635) were cultured in a humidified 37°C incubator with 5% CO_2 using high glucose DMEM media containing GlutaMAX™ and pyruvate (Gibco) supplemented with 10% heat-inactivated FCS (Gibco), 100 U/mL penicillin and 100 μg/mL streptomycin (Gibco). Cells were seeded on 15 cm dishes 18-24 hours prior to harvest to ensure an 80–90% confluency was reached at the time of collection.

METHOD DETAILS

Selective ribosome profiling

Purification of NAC-bound RNCs

NAC-bound RNCs were purified from a cell lysate or from sucrose cushion purified ribosomes after *in vivo* crosslinking to capture nascent chain-independent ($SeRP_{ribo}$) or nascent chain-dependent ($SeRP_{NC}$) interactions, respectively.

For the $SeRP_{ribo}$ assay, HEK293-T cells were harvested from 2-3 plates by detachment with ice-cold 1x PBS supplemented with 100 μg/mL cycloheximide and 12 mM $MgCl_2$, then pelleted by centrifugation. Cells were lysed in lysis buffer (20 mM Tris, pH 8.0, 140 mM KCl, 1 mM PMSF, 12 mM $MgCl_2$, 0.5% NP-40, 100 μg/mL cycloheximide, 25 U/mL DNase1 (Roche), 1x protease inhibitor cocktail (complete EDTA free, Roche)). This experiment was performed with a lysis buffer containing either 70 mM (rep1) or 140 mM KCl (rep2) to account for potential salt sensitivity of NAC association. Both datasets were highly correlated, showing a lack of salt sensitivity within this concentration range (Figure S1N, R2 = 0.979). The lysate was cleared by centrifuging for 5 min at 20,000 *g* and 4°C, followed by five times trituration through a 23-G needle. The cleared lysate was digested with 550 U/mg RNA of RNase I (Ambion) at 4°C for 40 minutes after which the digest was stopped by adding Superase·In (Invitrogen). One part of the digestion reaction (following RNase I addition) was immediately subjected to immunoprecipitation (IP) by mixing with 70 μL of protein A Dynabeads (ThermoFisher), pre-coated with 10 μg of a homemade NACβ antibody, and incubated at 4°C for 40 minutes under rotation. NACβ was chosen as target for immunoprecipitation (IP) because this subunit contains the ribosomal anchor domain. The antigen-bound Dynabeads were washed four times with 280 μL cold washing buffer (20 mM Tris, pH 8.0, 140 mM NaCl, 1 mM PMSF, 0.5% NP-40, 100 μg/mL cycloheximide, 12 mM $MgCl_2$) and shock-frozen in liquid nitrogen. For isolation of TT samples, the remaining of the digestion reaction was pelleted by sucrose cushion centrifugation (25% (w/v) sucrose, 20 mM Tris, pH 8.0, 140 mM KCl, 12 mM $MgCl_2$, 1 mM PMSF, 100 μg/mL cycloheximide) at 75,000 rpm for 90 min at 4°C (S120-AT2 rotor, Sorvall Discovery M120 SE Ultracentrifuge), and resuspended in lysis buffer.

For the $SeRP_{NC}$ experiment, HEK293-T cells grown in 10–13 plates were harvested and subjected to *in vivo* crosslinking with 1 mM DSP (Thermo Fisher) prior to cell lysis as described in reference[75]. Samples were lysed and digested as previously described for the $SeRP_{ribo}$ and subjected to sucrose cushion purification at the same conditions as used for the $SeRP_{ribo}$ TT isolation. A fraction of the resuspended ribosomal pellets was set aside as the TT fraction, while the remaining sample was subjected to IP using either a homemade NACα or NACβ antibody. IP samples were mixed with 200 μL protein A dynabeads pre-coated with 18 μg of NACα-antibody (homemade) or 18 μg of NACβ-antibody (homemade), respectively, and incubated overnight at 4°C under rotation. The antigen-bound dynabeads were washed three times with 800 μL cold high-salt washing buffer (20 mM Tris, pH 8.0, 650 mM NaCl, 1 mM PMSF, 0.1% NP-40, 100 μg/mL cycloheximide, 12 mM $MgCl_2$) and shock frozen in liquid nitrogen.

SolubleRP

Cells were harvested as previously as described above ($SeRP_{ribo}$ assay) from five 15 cm dishes per replicate. Cells pellets were resuspended in 1 mL ice-cold SolubleRP-lysis buffer (50 mM HEPES pH 7.0, 10 mM $MgCl_2$, 140 mM KCl, 0.1 mg/mL cycloheximide, 0.02 U/μl DNaseI (Roche), 2 μg/mL E64, 5 μg/mL Leupeptin, 8 μg/mL Pepstatin and 40 μg/mL Bestatin). Resuspended cells were frozen in liquid nitrogen as droplets and stored at -80°C until lysis by mixer milling (2 min, 30 Hz, Retsch) under cryogenic conditions. Samples were thawed for 2 min at a 30°C water bath and RNA digestion was carried out using 650 U RNase I (Ambion) per mg of RNA for 30 min at 4°C. The lysate was then split into two halves to generate the soluble translatome and the TT. For the soluble translatome sample, the lysate was centrifuged twice at 16,000 g for 15 min, both times collecting the supernatant. For the total translatome sample, NP-40 was added to the lysate to a final concentration of 0.1%, incubated for 5 min on ice, and then centrifuged at 500 g for 5 min at 4°C. The supernatant from this sample, as well as the soluble lysate were subjected to sucrose cushion centrifugation and pellet fractions were resuspended in SolubleRP-lysis buffer.

Onset of membrane association was calculated by fitting ribosome depletion from the soluble fraction to a sigmoidal profile, using a sigmoidal fitting strategy as previously described.[8] High confidence co-translationally translocated substrates were annotated according to the following criteria: (i) An RPKM value of at least 10 in the TT, (ii) A depletion in the ST compared to the TT (ST/TT < 1), (iii) Soluble ribosome depletion follows a sigmoidal shape and the onset of assembly can be determined. To ensure accuracy, we performed manual curation to correct cases where the sigmoidal fitting introduced errors in the assignment.

NACβ depletion using auxin-inducible degradation

Generation of the NACβ auxin inducible degradation system was previously described.[48] NACβ was chosen as target for degradation because this subunit contains the ribosomal anchor domain. Briefly, a GS linker-miniIAA7-GFP11 sequence was inserted at residue 176 of endogenous BTF3 via CRISPR/Cas9-mediated homology-directed repair in cells stably expressing AtAFB2. This system enables depletion of NACβ after 4.5 h of incubation with indole-3-acetic acid sodium (Santa Cruz, sc-215171).[48]

For ribosome profiling-based analysis of NACβ depletion, cells were seeded on 10 cm dishes 48 hours prior to harvest to ensure an 70-80% confluency at the time of collection. Cells were treated with 100 μg/mL indole-3-acetic acid sodium (Santa Cruz, sc-215171) for 9 hours prior to harvesting. Cells were collected from one 15-cm dish per condition, and lysates were clarified as described above. RNA concentration was measured using Qubit BR RNA assay and samples were digested with 3.5 U RNase I (Ambion) per μg of total RNA at 4°C for 30 minutes. Digestions were stopped by adding Superase·In (Invitrogen) and ribosomes were purified by sucrose cushion centrifugation as described above.

Ribosome profiling library preparation and sequencing

Ribosomal footprints were extracted using 15% denaturing urea polyacrylamide gel (Thermo Fisher Scientific). Gel slices containing footprints of 20-40 nt were excised and RNA was extracted using a crush-and-soak method. Gel slices were fragmented using gel breaker tubes and incubated in 0.5 mL of 10 mM Tris–HCl (pH 7.0) at 75 °C for 15 min with agitation. Gel debris was removed by centrifugation through Spin-X filter tubes (Corning) at 15,000 g for 2 min. RNA was precipitated overnight at -70 °C with 1 volume isopropanol, 0.1 volume 3 M sodium acetate (pH 5.5), and 2 μL GlycoBlue (Thermo Fisher Scientific), pelleted by centrifugation for 40 min at maximum speed, and washed with 80% ice cold ethanol.

Ribosome profiling libraries of SolubleRP and $SeRP_{NC}$ samples were generated using classical ribosome profiling protocols as described previously,[75,76] in combination with custom rRNA depletion at the level of cDNA.[8] Briefly, footprints were resuspended in 15 μL 10 mM Tris pH 7 and subjected for dephosphorylation by adding 2 μL 10x T4 polynucleotide kinase reaction buffer, 1 μL of murine RNase inhibitor, and 2 μL of T4 polynucleotide kinase. After incubating the samples for 1 h at 37°C the enzyme was heat-inactivated for 10 min at 75°C. RNA was subsequently precipitated by adding 500 μL10 mM Tris pH 7, 55 μL 3 M sodium acetate (pH 5.5), 2 μl GlycoBlue, and 0.55 mL isopropanol and incubating the samples overnight at -80°C. RNA was pelleted for 30 min at 20,000 g, 4°C, washed with 80% ice-cold ethanol, and resuspended in 10 μL 10 mM Tris pH 7. For linker ligation, RNA was denatured for 2 min at 80°C, mixed with 16 μL of 50% sterile-filtered PEG 8000, 4 μL of DMSO, 4 μL of 10x T4 RNA ligase 2 buffer, 2 μL of murine RNase inhibitor, 2 μL of 2 μM preadenylated linker 3-L1 (5'-/5rApp/ NNNNNATCGTAGATCGGAAGAGCACACGTCTGAA/3ddC/-3'), and 2 μL of T4 RNA ligase 2, and incubated for 2.5 h at 23°C. RNA was precipitated and ligation products were gel-purified on a 10% denaturing urea polyacrylamide gel as described above. Ligation products were resuspended in 10 μl 10 mM Tris pH 7 and subjected to reverse transcription. First, RNA samples were mixed with 1 μl of 25 μM reverse transcription primer (5'-/5Phos/NNAGATCGGAAGAGCGTCGTGTAGGGAAAGAG/iSp18/GTGACTGGAGTTCAGACGTGTGCTC-3'), 1 μL of 10 mM dNTP, and 1.5 μL of RNase-free water and incubated for 5 min at 65°C. Then, the reaction was combined with 4 μL 5x FS buffer, 1 μL of murine RNase inhibitor, 1 μL of 0.1 M DTT, and 1 μL of Superscript III and incubated for 30 min at 50°C. Reactions were quenched by adding 2.3 μL of 1 N NaOH and incubating for 15 min at 95°C. Reverse transcription products were then gel-purified on a 10% denaturing urea polyacrylamide gel as described above and resuspended in 15 μl 10 mM Tris pH 8. Circularization was performed by adding 2 μL of 10x CircLigase buffer, 1 μL of 1 mM ATP, 1μL of 50 mM $MnCl_2$, and 1 μL of CircLigase and incubating for 2 h at 60°C. After 1 h of incubation, an additional 1 μL of CircLigase was added to each sample. The enzyme was heat-inactivated by incubating for 10 min at 80°C. rRNA fragments were depleted from ribosome footprint libraries by hybridization of custom biotinylated reverse complement DNA oligonucleotides (developed in collaboration with siTOOLs Biotech, Table S4 in reference[8]), followed by a pull-down via magnetic Streptavidin beads (NEB). 10 μL of circularized cDNA was combined with 2 μL of the 20 μM rRNA depletion oligo pool, 2 μL 20x SSC buffer (3 M NaCl, 0.3 M sodium citrate), and 6 μL RNase-free water. For hybridiziation, samples were denatured at 99 °C for 90 s, followed by slow cooling to 37 °C at 0.1 °C/s and a 15-min incubation at 37 °C. 12.5 μL of Streptavidin beads were washed three times with 1x washing buffer (20 mM Tris pH 7, 500 mM NaCl, 1 mM EDTA, 0.05 % Tween 20), resuspended in 10 μL of the same buffer, and mixed with the hybridized sample. After incubating for 15 min at 37°C, rRNA-bound biotinylated oligos were captured magnetically and removed from the sample. The rRNA-depleted cDNA was precipitated by adding 500 μL 10 mM Tris pH 8, 32 μL 5 M NaCl, 1 μL 0.5 M EDTA, 0.55 mL isopropanol, and 2 μL GlycoBlue and incubating overnight at -80°C.

Ribosome profiling libraries of $SeRP_{ribo}$ were prepared using the NEXTflex Small RNA-Seq Kit v3 (PerkinElmer) following the manufacturer's instructions.

Ribosome profiling libraries for auxin depletion experiments were generated using a newly developed protocol as described in reference[77]. Briefly, purified RNA footprints were first dephosphorylated by resuspending the washed pellet in 4 μL of a PNK reaction mix (1x PNK buffer, 3.2 U PNK, 16 U murine RNase inhibitor) and incubating for 1 h at 37 °C. PNK was heat inactivated at 75 °C for 10 min. L1 ligation was performed by adding 4 μL of the L1 ligation mixture (1x RNA ligase buffer, 1 μM pre-adenylated L1 (5′-phosphate-NNNNNAGATCGGAAGAGCACACGTCT-GAACTCCAGTCAC-3′-TEG-biotin), 80 U T4 RNA Ligase 2 truncated, 30% PEG-8000) and incubating at 22 °C for 2 h. Unligated L1 was removed by treating with 25 U deadenylase and 45 U RecJf at 37 °C for 30 min, followed by heat inactivation at 75 °C for 10 min. The reaction was then combined with 2 μL of magnetic streptavidin Dynabeads pre-equilibrated in 50 μL BW buffer (10 mM Tris pH 7.0, 500 mM NaCl, 1 mM EDTA, 0.05% Tween-20) and incubated for 10 min. Beads were separated magnetically, the supernatant removed, and washed twice with 200 μL BW buffer and twice with 200 μL mild wash buffer (10 mM Tris pH 7.0, 0.05% Tween-20) at 50 °C. Washed beads were resuspended in 4 μL phosphorylation mix (1x PNK buffer, 3.2 U PNK, 1 mM ATP, 0.6x mild wash buffer) and incubated at 37 °C for 1 h. Next, 4 μL of L2 ligation mix (1x RNA ligase buffer, 1 μM L2 (5′-FAM-CTCTTTCCCTACACGACGCTCTTCCGATCT-NNNNNCrCrCrCrCrC-3′-OH), 1 mM ATP, 12 U RNA Ligase 1, 30% PEG-8000) was added and incubated at 37 °C for 1 h. Beads were magnetically separated, washed once with 50 μL mild wash buffer, and resuspended in 8 μL of the same buffer. RT primer annealing was performed by adding 3 μL of RT1 mix (6.7 μM RT primer (5′-FAM-GTGACTGGAGTTCAGACGTGTGCT-3′-OH), 3.3 mM each dNTP) and incubating at 65 °C for

5 min, followed by cooling on ice. Reverse transcription was carried out by adding 5 μL RT2 mix (3 μL First Strand buffer, 1 μL 100 mM DTT, 1 μL SuperScript III) and incubating at 50 °C for 30 min. Afterward, beads were magnetically separated, the supernatant removed, washed once with 50 μL mild wash buffer, and finally resuspended in 30 μL mild wash buffer. cDNA samples were stored at -20 °C until PCR amplified.

cDNA samples prepared with the different protocols were then amplified by PCR and the resulting construct was purified on a 6% PAGE-TBE gel and extracted as described for the ribosomal footprints, including isopropanol precipitation. Isopropanol-precipitated samples were resuspended in 12 μl 10 mM Tris (pH 7.0) and used for the preparation of the sequencing multiplex. All libraries were sequenced on a NextSeq550 (Illumina) according to the manufacturer's protocol. Raw sequencing data was processed using standard pipelines as described previously,[8] but keeping multimapped reads using star option '–outFilterMultimapNmax 20'. Importantly, unique molecular identifiers (UMIs) included in the linkers were used to remove PCR duplicates. Additional details on data processing, including command-line parameters and sample-specific information, are available at GEO under accession number GSE290865.

Two independent replicates were prepared for each condition. ST replicates of each experiment were highly correlated (Figure S1N). The profiles obtained in the $SeRP_{NC}$ experiments were virtually identical, independently of whether the IP was targeting NACα or NACβ (Figure S1N). We therefore selected the NACβ for further analysis, since this NAC subunit contains the ribosome anchor.

Bioinformatic analysis

Single gene and metagene enrichment profiles

Single gene profiles show the position-wise 95% binomial confidence interval (CI) -according to Agresti and Coull- of the ST/TT enrichment corrected for library size. Annotated ribosome-exposed protein domains are shown by applying a 30-residue tunnel correction to account for their emergence from the exit tunnel. For metagene analysis, position-wise enrichments of ST over TT were calculated using a sliding window of 12 codons. Expression levels were used to normalize the contribution of each gene by dividing the read density at every position by the average read density of the gene in the TT. Genes with a coverage lower than 0.1 reads/codon were excluded. Metagene profiles were plotted as solid lines with a 95% confidence interval as previously described (https://github.com/ilia kats/RiboSeqTools and reference[8]). For both single and metagene plots, the two replicates of each experiment were merged into one dataset, increasing the read density and coverage. ST/TT enrichments were calculated as the ratio between the RPM of a given gene in the ST and TT.

Identification of NAC binding periods

To identify NAC binding periods, a 30-codon smoothing was applied to the ST and TT raw data to reduce experimental noise. Only proteins with a RPKM value higher than 10 in the TT were included in the analysis. Then, the 95% CI -according to Agresti and Coull- of the ST/TT enrichment was calculated for each individual replicate and used to define NAC-bound positions using a simple heuristic based on a threshold enrichment value of 1.5. Each position in a gene was assigned a value as follows:

High-confidence binding, if the lower CI was above 1.5 .0.2: Low-confidence binding, if the CI overlapped the 1.5 threshold.

0: Not bound, if the upper CI bound was below the threshold.

Positions with an average value across the two replicates higher that 0.6 were considered binding periods. Binding periods shorter than 10 consecutive codons were excluded. Proteins with at least one NAC binding period in the $SeRP_{NC}$ were considered positive NAC substrates.

Annotation of the human proteome

Human protein domains were extracted from Manriquez-Sandoval and Fried,[78] and analyzed based on the ECOD annotation of protein topologies and architectures. The DSSP annotation of the human proteome was performed using all human Alphafold derived .cif files (UP000005640_9606_HUMAN_v4) considering regions with a pLDDT value > 70. TMDs, SP and mitochondrial targeting sequences (MTS) were retrieved from UniprotKB.[79] TMDs associated with co-translational targeting were defined as the TMD emerging from the exit tunnel closer to the onset of membrane association. Mitochondrial protein location (matrix, IMP, OMP or intermembrane space) was extracted from MitoCarta3.0.[80]

Annotations of human protein subcellular localizations were extracted from the UniprotKB, Gene Ontology, and LOCATE.[79,81,82] If no information was present for the human protein, the localization of mouse and rat orthologues were instead retrieved. To identify cytonuclear proteins, the database was screened for the following terms: 'cytosol', 'nucleoplasm', 'nucleus', 'cytoplasm', 'nucleoli', 'nucleolus', 'perinuclear region of cytoplasm'. Proteins were annotated as cytonuclear if they contained at least one of these terms and no TMD was annotated in UniprotKB. To avoid multiple annotations for the same protein, annotations were hierarchically ranked as following: (i) Annotations from different organisms were ranked human > mouse > rat; (ii) Annotations from different databases within the same organism were ranked UniprotKB > Gene Ontology > LOCATE.

Analysis of sequence features

Residue hydrophobicity was calculated using Kyte-Doolittle hydrophobicity scale.[46] α-helical hydrophobic moment (μH) of protein sequences was used as a measure of amphiphilicity of α-helices and was calculated as described by Eisenberg et al.[47] using a sliding window of 11 residues. α-helical and β-sheet content was calculated based on the previously mentioned DSSP annotation derived from Alphafold derived structures of human proteins.[19,20] Protein disorder was calculated with IUPRED 2.0 using default settings.[67] For the metagene analysis of protein features aligned to the onset of NAC binding periods position-wise mean confidence intervals

were calculated for each feature. Background profiles were generated by randomly sampling 5 positions in each of the analyzed genes.

Gene ontology and frequency enrichments

Gene ontology terms were analyzed with the Functional Annotation Tool of DAVID v6.8 (Database for Annotation, Visualization and Integrated Discovery).[66] The analysis was performed with default settings, and custom datasets were uploaded as background sets tailored to the tested enrichment. GO terms with an adjusted p-value < 0.05 were considered significantly enriched. Simple frequency enrichments were calculated for domain topology and architecture by calculating fold enrichment, and statistical significance was tested using Fisher's exact test.

Position-specific enrichment of DSSP secondary structure and amino-acid identity

DSSP secondary structure assignment and amino acid identity of the ribosome-proximal 60 residues at the onset of NAC binding periods were extracted and compared with a random background generated by randomly sampling 5 positions in each of the analyzed genes. Enrichment analysis were performed using Two Sample Logo webpage[68] using default settings.

Protein Preparation for smTIRF microscopy

NAC Purification

The human NAC heterodimer, comprising N-terminally 6×His tagged NACα and NACβ with the S57C mutation for labeling, was expressed using a pET28b plasmid in *E. coli* BL21 (DE3) cells, as described.[38] Cells were grown at 37°C to OD_{600} 0.6, at which the temperature was reduced to 18°C, and overexpression was induced with 1 mM IPTG for 16 hours.

Harvested cells were lysed by sonication in NAC Lysis Buffer (50 mM KHEPES, pH 7.5; 1 M NaCl; 6 mM β-mercaptoethanol; 30 mM imidazole; 10% glycerol) supplemented with 1×ProBlock Gold Protease Inhibitor Cocktail (GoldBio) and 1 mM AEBSF. The lysate was clarified by centrifugation at 18,000 rpm for 1 hour in a JA-20 rotor (Beckman Coulter). The clarified lysate was incubated with Ni Sepharose High-Performance resin (Cytiva) at a ratio of 1 ml resin per liter of culture for 1 hour with gentle rotation at 4°C. The resin was subsequently washed in batches with 50 column volumes (CVs) of NAC Lysis Buffer. Bound proteins were eluted twice with 5 CVs of NAC Elution Buffer (50 mM KHEPES, pH 7.5; 100 mM NaCl; 500 mM imidazole; 1 mM TCEP; 10% glycerol). Eluted protein was incubated with PreScission Protease overnight at 4 °C with gentle rotation. Protein was further purified on a Mono Q 10/100 GL anion-exchange column (Cytiva) in NAC Buffer (50 mM KHEPES, pH 7.5; 1 mM TCEP; 10% glycerol) using a linear gradient of 100 mM – 500 mM NaCl over 10 column volumes. Peak fractions were pooled and concentrated using a 10 kDa molecular weight cutoff (MWCO) centrifugal concentrator (Amicon). The purified protein was aliquoted, flash-frozen in liquid nitrogen, and stored at −80 °C. NAC concentration was determined using an extinction coefficient of ε_{280} = 2,980 M^{-1} cm^{-1}.

NAC labeling

NACα/NACβ(S57C) was labeled with maleimide-Cy3B (Cytiva). The protein was exchanged into labeling buffer (50 mM KHEPES, pH 7.5; 100 mM NaCl; 1 mM TCEP; 20% glycerol) and incubated with a 5-fold molar excess of dye for 2 hours at room temperature. Excess free dye was removed using a G-25 Sephadex size exclusion column (GE Healthcare). Fractions containing labeled NAC were identified via SDS-PAGE, pooled, and concentrated to a final concentration of 150 μM.

RNC_{hRPL4} Purification

PCR and in vitro transcription

DNA fragments encoding, from 5' to 3', the T7 promoter, IRES, 3X-FLAG, SUMO, and the nascent chain at defined lengths were generated by PCR. All amplicons contained an additional CAC at the 3' end to generate a C-terminal Val that stabilizes the stalled ribosome-nascent chain complex. Amber codons were inserted in the RPL4 coding sequence to allow for non-natural amino acid incorporation and dye labeling. PCR products were purified using the QIAquick PCR Purification Kit (Qiagen, cat no. 28104) and used for *in vitro* transcription using home-made T7 polymerase and the MegaScript protocol. 5 mM 5'-biotin-GMP (TriLink) was included during transcription to incorporate a biotin at the 5'end of the mRNA. mRNA was partially purified by precipitation in 3M LiCl at –20 °C for an hour, followed by wash with 200 uL of ice-cold 70% ethanol. RNA pellet was resuspended in Ultrapure d.d. water.

RNC labeling and purification

RNCs were generated by *in vitro* translation in rabbit reticulocyte lysate (RRL, Green Hectares) supplemented with 1 μM *Methanosarcina mazei* pyrrolysine synthase (*Mm*PylRS, home-made), 10 mg/L *M. mazei* amber suppressor tRNA (*Mm*PyltRNA, home-made), and 100 μM axial-trans-cyclooct-2-en-L-lysine (TCOK, SiChem), for 30 minutes at 32 °C, as described.[38] Translation reactions were layered onto a high-salt sucrose cushion (50 mM KHEPES, pH 7.5, 1 M KOAc, 15 mM $Mg(OAc)_2$, 0.5 M sucrose, 0.1% Triton X-100, 2 mM DTT) at a 2:3 volumetric ratio and ultracentrifuged at 100,000 rpm for 45 minutes at 4 °C (TLA100.3 rotor, Beckman Coulter). Ribosomal pellets were resuspended in RNC buffer (50 mM KHEPES, pH 7.5, 150 mM KOAc, 2 mM $Mg(OAc)_2$) to a ribosome concentration of 1 μM and incubated with 1 μM tetrazine-conjugated Atto647N dye (Jena Biosciences) for 30 minutes at 25 °C to enable Diels-Alder cycloaddition of the fluorescent dye to TCOK. For double labeling of the nascent chain, resuspended ribosome fraction was incubated with 1 μM tetrazine-conjugated Atto647N (Jena Biosciences) and 1 μM tetrazine-conjugated Cy3B (AAT Bioquest) for 30 minutes at 25 °C. The following RNC purification steps were analogous for both single- and double-labeled RNCs.

Labeled RNCs were incubated with anti-DYKDDDK magnetic agarose beads (Pierce) pre-equilibrated in RNC Buffer for one hour at 4 °C with constant rotation. Beads were washed sequentially with 10 CVs of RNC buffer containing 300 mM KOAc, 10 CVs of RNC buffer with 0.1% Triton X-100, and 10 CVs of RNC buffer alone. RNCs were eluted using 1.0 mg/mL 3×FLAG peptide (DYKDDDK) for

30 minutes at 4 °C with constant rotation. The eluate was treated with 1 μM 3C protease (GoldBio) at 25 °C for at least one hour. Purified RNCs were sedimented through a high-salt sucrose cushion at a 2:3 volumetric ratio by ultracentrifugation at 100,000 rpm for 30 minutes at 4 °C (TLA120.2 rotor, Beckman Coulter). The pellet was resuspended in Assay Buffer (50 mM KHEPES, pH 7.5, 150 mM KOAc, 5 mM $Mg(OAc)_2$, 0.04% Nikkol, 2 mM DTT) to a final ribosome concentration of ~100 nM. Fluorescently labeled nascent chains were validated by SDS-PAGE and fluorescence imaging (Typhoon biomolecular imager, Cytiva). Labeled RNCs were snap-frozen in liquid nitrogen and stored at −80 °C. Following SDS-PAGE and fluorescence imaging, double labeling of the RNCs was verified under the smTIRF setup, where the doubly labeled RNCs were identified as immobilized spots with both fluorescent dyes colocalized.

Single-molecule TIRF microscopy

Quartz imaging slides and coverslips were aminosilanized using Vectabond (Vector Laboratories) and coated with biotin-PEG (Laysan Bio). The slides were passivated in Passivation Buffer (1× Tween-20, 1 mg/mL BSA) for at least 1 hour at 25 °C, washed with 50 mM KHEPES, pH 7.5, and incubated with 0.5 mg/mL NeutrAvidin (ThermoFisher) for 10 minutes. Excess NeutrAvidin was removed by washing with Imaging Buffer, comprising the Assay Buffer supplemented with 1 mg/mL BSA and the oxygen scavenging system[83] (4 mM Trolox, 2.5 mM protocatechuic acid (PCA), and 50 nM protocatechuate-3,4-dioxygenase (PCD, Sigma)).

Biotinylated RNCs were diluted to 1.5 nM in Imaging Buffer and immobilized on NeutrAvidin-functionalized slides for 10 minutes at 25 °C. Following that, the slides were flushed with 2 nM Cy3B-labeled NAC in Imaging Buffer. Images were captured using MicroManager on a custom-built (TIRF) microscopy setup.[84] The presence of Atto647N-labeled RNCs was verified by excitation at 635 nm. Single-molecule fluorescence measurements were conducted with donor excitation at 532 nm (Cy3B) in single-excitation mode, with simultaneous detection of donor and acceptor channels at a temporal resolution of 50 ms.

Single-molecule FRET data analysis

Donor and acceptor channels were aligned and analyzed using iSMS software.[69] Raw donor and acceptor fluorescence intensities were corrected for background noise, the γ factor that accounts for differences in dye quantum yield, and donor leakage into the acceptor channel. Apparent FRET efficiencies (E_{app}) were calculated using Equation 1:

$$E_{app} = \frac{I_{DD}}{I_{DD}+I_{AD}} \quad \text{(Equation 1)}$$

where I_{DD} and I_{AD} are the corrected fluorescence intensities of the donor and acceptor dyes, respectively, upon excitation of the donor. Each data point represents a single FRET event, limited by temporal resolution of the image acquisition system and equals 50 ms.

The FRET traces for the same experimental group across all experiments were extracted from iSMS, truncated at the photobleaching events, and pooled for HMM[85] using the *hmmlearn* algorithm package in Python. The number of FRET states was determined using the Bayesian Information Criterion (BIC) and Akaike Information Criterion (AIC), by using the functions bic() and aic() from the *hmmlearn* package. The BIC and AIC values were calculated for individual models with 1-5 FRET states. The model with the smallest number of states with low BIC and AIC values was selected to prevent overfitting. In all cases throughout this study, the optimal number of states was determined to be three.

HMM analysis was then repeated with the number of states set to 3 and the number of iterations increased to 100 000 for a more refined fitting (HMM parameters: number of states = 3, covariance structure = full, number of interactions for model fitting = 100,000, convergence tolerance = 1e-5, parameters updated during training = stmc, inference algorithm = Viterbi, minimal state duration = 3 frames).This procedure allowed for determination of the mean FRET efficiency values for each state and its standard deviation (Table S5), which were used to fit smFRET histograms using Equation 2:

$$PDF = \sum_{i=1}^{n} A_i \cdot \frac{1}{\sigma_i\sqrt{2\pi}} e^{-\frac{1}{2}\left(\frac{E-\mu_i}{\sigma_i}\right)^2} \quad \text{(Equation 2)}$$

where PDF is the probability density function, n is the number of FRET states detected and was set to 3 (determined by HMM), A_i is the weight of the i^{th} Gaussian, and σ_i and μ_i are the standard deviation and center (determined by HMM) of the i^{th} Gaussian.

To evaluate the residence time of NAC on RNCs, the cumulative fluorescence intensity ($I_{cumulative}$) for the dye pairs in experiment 2 was calculated for each trace using Equation 3:

$$I_{cumulative} = I_{AD} + \gamma \cdot I_{DD} \quad \text{(Equation 3)}$$

Colocalization of labeled NAC and RNCs was identified when $I_{cumulative}$ exceeded background noise. Two-state HMM was used to distinguish bound and dissociated states of NAC, allowing the determination of dwell times (t) for individual colocalization events. The cumulative probability distribution of t was fit to the two-exponential decay function in Equation 4:

$$f(t) = A_{fast} \cdot e^{-k_{fast} \cdot t} + A_{slow} \cdot e^{-k_{slow} \cdot t} \quad \text{(Equation 4)}$$

in which A_{fast} and A_{slow} are the amplitudes of the fast- and slow-dissociating NAC populations, and k_{fast} and k_{slow} are their respective dissociation rate constants.

Cryo-EM sample preparation

Design of RPL4(1-158)-XBP1u plasmid

The plasmid encoded a T7 promoter, EMCV internal ribosome entry site, EGFP, SENP-EuB protease cleavage site, the first 158 amino acids of human RPL4, XBP1u translational arrest peptide and a 30-nt polyA tail, in the pT7CFE1-Chis vector (Thermo Fischer Scientific).

Due to partial folding of the 26 amino acid-long XBP1u peptide in the polypeptide exit tunnel,[86] its length is approximately equivalent to that of a 22 amino acid unfolded polypeptide chain. Therefore, the nascent chain (after GFP cleavage) mimics 180 amino acid-long RPL4, assuming that the C-terminal 30 amino acid stretch of RPL4 in the polypeptide exit tunnel is unfolded.

In vitro *transcription of mRNA [RPL4(1-158)-XBP1u]*

Linearized DNA template for *in vitro* transcription, which encompassed the T7 promoter at the 5′ end and the polyA tail at 3′ end, was generated by PCR using the Q5 DNA polymerase (NEB). After treating the PCR reaction with DpnI (NEB), the template was purified using the QIAquick PCR purification kit (Qiagen). The *in vitro* transcription reaction consisted of 1.15 mg/ml homemade T7 polymerase, 12 nM DNA template, 5 mM NTPs, 30 mM $MgCl_2$, 40 mM Tris-HCl pH 7.6, 1 mM DTT, 2 mM spermidine, and 0.1 U/μL RNaseOUT™ Recombinant Ribonuclease Inhibitor (Thermo Fischer Scientific). The reaction was carried out at 37 °C for 2 h, followed by digestion of the DNA template by 0.04 U/μL of RNase-free DNase I (Qiagen). mRNA was precipitated by ½ reaction volume of 7M LiCl at -20 °C for 1 h and pelleted by centrifugation for 15 min at 13,000 rpm and 4 °C. The pellet was washed with 70% ethanol and centrifuged again, then air-dried. The mRNA was resuspended in pure water and stored at -20 °C.

Protein purification

The human NAC heterodimer, containing NACα with an N-terminal 6x His tag and TEV protease cleavage site, was expressed in *E. coli* BL21 (DE3). Transformed bacteria were grown in 2YT containing kanamycin (50 μg/mL) at 37 °C to an optical density (OD_{600}) of 0.7, followed by induction with 1 mM isopropyl β-d-1-thiogalactopyranoside (IPTG) and incubation overnight at 18 °C. Bacteria were lysed by sonication in buffer A (50 mM HEPES pH 7.6, 800 mM KCl, 40 mM imidazole, 10% glycerol), supplemented with 100 μM PMSF, 2 μM E−64, 10 μM Leupeptin, 10 μM Bestatin, 1 μM Pepstatin A, 10 μg/mL Aprotinin, and a pinch of DNase I. The lysate was centrifuged in an SS-34 rotor (Sorvall) for 45 min at 20,000 rpm and 4 °C. The clarified supernatant was loaded on a HisTrap HP column (Cytiva), washed with buffer A, and eluted directly on a HiTrap Q HP column (Cytiva) using a linear gradient from buffer A to 100% buffer B (50 mM HEPES pH 7.6, 100 mM KCl, 500 mM imidazole, 10% glycerol) over 10 column volumes. The protein was then washed with buffer C (50 mM HEPES pH 7.6, 100 mM KCl, 10% glycerol), and eluted with a linear gradient from buffer C to 100% buffer D (50 mM HEPES pH 7.6, 800 mM KCl, 10% glycerol) over 10 column volumes. Peak fractions were pooled and incubated with homemade TEV protease overnight at 4°C. The protein was loaded on a HisTrap HP column and washed with buffer A, followed by a linear gradient from buffer A to 100% buffer B over 10 column volumes. NAC was collected in the flow-through, concentrated and buffer exchanged to 50 mM HEPES pH 7.6, 150 mM KOAc, 10% glycerol, 1 mM TCEP, using a 30 K MWCO centrifugal filter (Amicon). Aliquots were flash-frozen in liquid nitrogen and stored at -80°C.

GADD34 was purified as described in reference[65]. Briefly, GADD34 was recombinantly expressed in *E. coli* BL21 (DE3) pLysS. Bacteria were grown in TB containing ampicillin (100 μg/mL) at 37 °C, and protein expression was induced with 1 mM IPTG at $OD_{600} \approx 5$. After 6 h, cells were harvested, flash-frozen, and stored at -80 °C. Bacteria were lyzed by sonication in lysis buffer (50 mM HEPES pH 7.6, 500 mM KCl, 5 mM $MgCl_2$, 10 mM imidazole, 10% glycerol, 2 mM TCEP, 100 μM PMSF, 2 μM E−64, 10 μM Leupeptin, 10 μM Bestatin, 1 μM Pepstatin A, 10 μg/mL Aprotinin, DNase I, lysozyme). Insoluble material was removed by centrifugation (20,000 rpm, 1 h, 4 °C). The clarified lysate was loaded on a HisTrap HP column (Cytiva), washed with buffer A (50 mM HEPES pH 7.6, 150 mM KCl, 10% glycerol, 40 mM imidazole, 1 mM TCEP), and protein was eluted with a linear gradient to buffer B (50 mM HEPES pH 7.6, 100 mM KCl, 10% glycerol, 500 mM imidazole, 1 mM TCEP). The protein was then bound to a HiTrap Q HP column (Cytiva), washed with low-salt buffer (50 mM HEPES pH 7.6, 150 mM KCl, 10% glycerol, 1 mM TCEP), and eluted with a linear gradient to high-salt buffer (50 mM HEPES pH 7.6, 1 M KCl, 10% glycerol, 1 mM TCEP). The first elution peak was concentrated (30 K MWCO Amicon) and subjected to preparative size-exclusion chromatography using a HiLoad 16/60 Superdex 75 column (Cytiva) equilibrated in 10 mM HEPES pH 7.6, 30 mM KCl. Fractions corresponding to the void volume were concentrated, aliquoted, flash-frozen, and stored at -80 °C.

Design and purification of NAC mutant (NAC_{mut})

To test whether the identified hydrophobic patch may contribute to NAC's interactions with nascent chains and its effect on folding, we mutated selected residues of the hydrophobic patch to polar uncharged residues. Residues I128 in NACα, and V53 and L83 in NACβ, were selected for mutagenesis based on their proximity to the extra nascent chain density, conservation of their hydrophobic character,[87] and positioning away from the NACα/β dimerization interface. The mutations NACα/I128N, NACβ/V53S and NACβ/L83N increase hydrophilicity of the NAC surface while maintaining the approximate size of the side chains. The combination of mutations was predicted by FoldX[70] to preserve the stability of NAC alone and in the context of 60S/RPL4 nascent chain. The BuildModel function of FoldX[70] was used to simulate the mutant NAC structure for visualization purposes (Figure S7B). NACα I128N/ NACβ L83N V53S complex was purified as described for wild-type NAC. Copurification of NACβ with NACα indicated that the mutations do not perturb NAC dimerization.

Generation and purification of RNC (RPL4(1-158)-XBP1u)

RPL4 RNC were generated using the human *in vitro* translation system as described previously.[65] The *in vitro* translation reaction consisted of 75% (v/v) human cell extract, 0.01 mg/ml GADD34, 100 nM mRNA, 15 mM HEPES pH 7.0, 120 mM KCl, 0.9 mM $MgCl_2$ and 20 mM creatine phosphatase. The reaction was incubated at 33 °C for 20 min.

RPL4 RNC were purified using GFP nanobody-conjugated magnetic beads and elution by GFP cleavage (tag off) as described previously[88] with the following modifications: The *in vitro* translation reaction was supplemented with 0.1% Triton X-100 and diluted to 1.2 mL with buffer 1T (50 mM HEPES pH 7.4, 100 mM KCl, 5 mM $MgCl_2$, 0.1% Triton X-100), followed by incubation with the GFP nanobody-conjugated magnetic beads for 1 h at 4 °C with rotation. Beads were washed twice with buffer 1T, twice with buffer 2T (50 mM HEPES pH 7.4, 500 mM KCl, 5 mM $MgCl_2$, 0.1% Triton X-100), and twice with buffer 1T. RNCs were eluted with 250 nM SENP-EuB SUMO protease (homemade) in buffer 1T by incubating for 20 min on ice; the elution was performed twice. The pooled elutions were clarified at 21,300 *g* for 1 min, followed by centrifugation in the TLA-55 rotor (Beckman Coulter) at 55,000 rpm for 2 h. The RNC pellet was resuspended in RNC buffer (50 mM HEPES pH 7.4, 100 mM KOAc, 5 mM $MgOAc_2$). Aliquots were flash-frozen in liquid nitrogen and stored at -80 °C.

Samples were taken throughout RNC generation and purification for analysis on 4-12% SDS PAGE gels (Millipore), followed by transfer using the eBlot™ L1 system (Genscript) and detection using a polyclonal GFP primary antibody (Invitrogen, A6455) and HRP-conjugated mouse anti-rabbit secondary antibody (Santa Cruz Biotechnology, sc-2357).

Reconstitution of RNC/NAC complex for cryo-EM

Prior to grid preparation, 100 nM RPL4 RNC was mixed with 1 μM NAC heterodimer and 0.02% octaethylene glycol monododecyl ether in RNC buffer. The mixture was incubated at 30 °C for 10 min, then placed on ice.

Cryo-EM methods

Grid preparation

Quantifoil R2/2 Cu 300 grids, coated with a homemade 1 nm thick layer of amorphous carbon, were glow-discharged for 15 s at 15 mA using the PELCO easiGlow Discharge cleaning system (Ted Pella). Grids were mounted into a Vitrobot MK IV (Thermo Fischer Scientific), preset to 4 °C and 100% humidity, and 5 μl of the RNC/NAC sample was applied on the grid. After 30 s, the grids were blotted for 4 s with a blot force of 15, then immediately plunge-frozen in a 1:2 mixture of ethane and propane.

Grids were imaged using a Titan Krios G3i transmission electron microscope at 300 kV, equipped with a BioQuantum imaging filter with the energy filter slit set to 20 e^-V, and a K3 direct electron detector (Gatan). Movies were collected in super-resolution counting mode, then binned to the physical pixel size during data collection. The nominal magnification was 81000x, corresponding to a physical pixel size of 1.047 Å/pixel. During collection, exposure was set to reach a total electron dose of 50 $e^-/Å^2$ and the defocus values ranged from -0.7 μm to -2.2 μm in steps of 0.3 μm. EPU 3.6.0.3689 (Thermo Fischer Scientific) was used for automated data collection. 9,751 and 10,444 movies were collected in two independent sessions from two different RNC and cryo-EM grid preparations.

Cryo-EM data processing

CryoSPARC Live was used to motion-correct, dose-weigh and sum movie frames into micrographs, followed by estimation of CTF parameters (Figure S7E). Some micrographs were excluded based on the maximum resolution of the CTF fit, the ice thickness and total motion. Particles were picked either with an 80S template (low-pass filtered to 40 Å) in CryoSPARC or using a blob picker (circular, 250 - 350 Å) in CryoSPARC Live. Particles were extracted using a box size of 560 pixels and subsequently Fourier cropped to a box size of 186 pixels. All subsequent processing was performed in CryoSPARC[71] for both datasets. After 2D classification, ribosome-like classes were selected for further processing (371,689 particles in dataset 1; 503,918 particles in dataset 2). An *ab initio* reconstructed 80S ribosome was used as a template for heterogeneous refinement, which separated a class of leading ribosomes with a P-site tRNA and no downstream ribosome (207,513 particles in dataset 1; 233,286 particles in dataset 2). As these represent RNCs that are translationally arrested at the programmed site and bear the designed nascent chain, these particles were selected for further processing and homogenously refined. The particles were re-extracted with a box size of 560 pixels and homogenously refined, with optimization of per-particle defocus and per-group CTF parameters. Due to the high similarity of cryo-EM maps from the two datasets, particles were merged at this point and homogenously refined. 3D classification with a mask around NAC was used to select particles with a well-defined NAC globular domain (104,588 particles; 24% of leading ribosomes). These were homogenously refined with per-particle defocus optimization, and subsequently non-uniformly refined to an overall resolution of 2.7 Å (EMD-56598). The map was further locally refined with masks covering either the 40S head or the 40S body (deposited as EMD-56583 and EMD-56582, respectively) for the purposes of model building only.

Model building

For molecular interpretation of the 2.7 Å EM map calculated for the NACα/β-bound 80S ribosome stalled on the RPL4-XBP1u mRNA construct, available structures for the human small ribosomal subunit (8PPL), the large subunit (9GMO), the tRNA(Met)-bound XBP1u nascent chain (from 6R7Q) and a model of human NACα/β (from 7QWR) were docked as rigid bodies using CHIMERAX.[72] The composite model was the manually readjusted in COOT[73] using available high-resolution structures of human (8QOI) and rabbit (7O7Y) 80S ribosomes as a guide.

The yeast tRNA(Met) sequence was altered to the human tRNA-Met-CAT-1-1 including modifications (available from the GtRNAdb on https://gtrnadb.ucsc.edu/)[89] and readjusted. The C-terminal portion of the nascent chain could be CA-traced from residues 151–184, with unambiguous assignment of protein side chains from residues 156–171 (Figure 5C) and from Ala179 to the tRNA-attached Met184:

MACARPLISVYSEKGESSGKNVTLPAVFKAPIRPDIVNFVHTNLRKNNRQPYAVSELAGHQTSAESWGTGRAVARIPRVRGGGTHRS GQGAFGNMCRGGRMFAPTKTWRRWHRRVNTTQKRYAICSALAASALPALVMSKGHRIEEVPEL*PLVVEDKV*QKDPVPYQPPFLCQW *GRHQCAWKPLM*

Protein sequence of the nascent chain construct, with the N-terminal portion corresponding to RPL4 residues 1–158 and the C-terminally fused XBP1 stalling sequence underlined. The traced portion (residues 151–184) is marked in italics, and the tRNA(-Met)-attached methionine in bold.

This, together with careful inspection of the codon-anticodon base pairing and the nucleotide pattern of the tRNA(Met) anticodon stem-loop in a map focused on the small subunit, confirmed that the translation had been stalled by the XBP1u sequence at the expected position.

Real space refinement

The completed structure was refined for several cycles into the 2.7 Å EM map using real space refinement in PHENIX version 2.0_5936.[74] Custom restraints for modified rRNA and protein residues were generated using phenix.eLBOW,[74] PRODRG[90] or exported from COOT.[73] To stabilize good model geometry also in less well-ordered areas at the periphery of the 80S map, the model was initially refined with added hydrogens and using protein secondary structure, rotamer and Ramachandran as well as RNA base pair and stacking restraints. Real space difference maps were used to find and correct remaining discrepancies between the model and the EM map. During final cycles of refinement, hydrogens were removed from the model, and the secondary structure restraints were released except for the Ramachandran restraints for a better model-to-map fit. The structure was validated using MOLPROBITY,[91] revealing that the model displays excellent geometry and map correlation (Table S6). The resolution of the refined model vs. map FSC at a value of 0.5 (3.0 Å, masked) coincides well with the resolution determined between the map half-sets at the FSC=0.143 criterion (2.7 Å).

Single-molecule optical tweezers

Bacterial MBP with introduced cysteine residues was expressed in BL21 and affinity-purified using Amylose resin (New England Biolabs).[54] Human NAC heterodimer, comprising NACα and his-tagged NACβ, was co-expressed in BL21 and purified by Ni-NTA and MonoQ chromatography.[3] MBP was coupled to maleimide-modified 20-nt DNA oligos (biomers.net) via thiol-maleimide reaction, and hybridized to 1.3-kbp double-stranded functionalized DNA handles via an overhang approach.[54] This yielded a DNA-MBP-DNA construct, functionalized with biotin group at one end and digoxigenin at the opposite end. To create the first bead-construct connection, the construct was incubated with anti-digoxigenin antibody-coated polystyrene beads (diameter 2.1 μm, Roche) for 30 mins with rotary shaking at 4 °C in assay buffer (50 mM HEPES, 150 mM potassium acetate, 1 mM TCEP, pH 7.4). The second bead-construct connection was created by using neutravidin-coated polystyrene beads (diameter 2.1 μm, Spherotech). Single-molecule measurements were performed in the assay buffer with addition of an oxygen scavenging system (3 units mL^{-1} pyranose oxidase, 90 units mL^{-1} catalase, and 50 mM glucose, all from Merck).

All single-molecule optical trapping measurements were performed using a C-Trap setup (Lumicks),[54,57] with a constant trapping laser intensity. In these measurements, the samples were introduced into separate channels of a pressure-controlled microfluidic flow cell. Following optical trapping of a bead pair, which contained an anti-digoxigenin-bead coupled to the MBP construct and a neutravidin-bead, the two beads were moved close to enable tether formation, verified by increase in force upon retraction. Single tethers were confirmed by the typical shape of the MBP unfolding profile with a large increase in extension due to unfolding of the MBP core and by the presence of the DNA overstretching plateau at 65 pN. The tethers were repeatedly stretched and relaxed, with the pulling and relaxation rates of the steerable trap of 0.1 μms^{-1} and 5 s waiting time at 0 pN, until tether breakage. For each molecule, the optical traps were calibrated by fitting a Lorenzian function to the power spectrum of the trapped bead pair.

Data were collected at 50 kHz and decimated to 500 Hz for the analysis. Segments of the force-extension curves were fit with two worm-like chain (WLC) models in series: an extensible WLC for the DNA contribution, and the Odijk approximation for an inextensible WLC for the protein component,[54,57] with rulers at 0 nm (fully folded MBP), 33 nm (folded core) and 129 nm (fully unfolded protein). First pulling curves were excluded from the analysis, as we aimed to study refolding from the unfolded state. Any tethers that did not show full unfolding in the first pulling cycle were excluded, as well as any molecules that did not display any core unfolding transitions.

Force-dependent lifetime analysis

Force-dependent lifetimes (Figure S8F) were extracted according to the procedure described by Dudko et al.[92] Unfolding-force distributions measured in constant pulling speed experiments are related to force-dependent lifetimes[92] $\tau(F)$ by Equation 5:

$$\tau(F) = \frac{\int_F^\infty p(f)df}{\dot{F}(F)p(F)}. \quad \text{(Equation 5)}$$

Here, $p(f)$ is the unfolding-force distribution and $\dot{F}(F)$ is the force-dependent loading rate.[92] The force-dependent loading rate was calculated using Equation 6:

$$\dot{F}(F) = v\left[\frac{1}{\kappa_s} + \frac{2\beta L_c l_p\left(1+\beta F l_p\right)}{3+5\beta F l_p + 8\left(\beta F l_p\right)^{\frac{5}{2}}}\right]^{-1} \quad \text{(Equation 6)}$$

where v is the pulling rate and Ks is the trap stiffness. The second term arises from the contribution of the flexible linkers[92]. The contour length L_c (798 ± 72 nm) and the persistence length l_p (39.1 ± 8.7 nm) were determined by the fitting procedure described above. Discrete unfolding-force histograms, containing N = 30 bins of width $\Delta F = 1.3$ pN, were transformed into force dependent lifetimes[92] using Equation 7:

$$\tau(F_j) = \left[\frac{\left(\frac{h_j}{2} + \sum_{m=j+1}^{N} h_m \right) \Delta F}{h_j \dot{F}(F_j)} \right]. \quad \text{(Equation 7)}$$

Here, F_j is the center of bin j and h_j the normalized number of counts in the jth bin.

QUANTIFICATION AND STATISTICAL ANALYSIS

No statistical methods were used to predetermine sample size. SeRP profiling experiments were performed in duplicate. The number of biological replicates, independent experiments, molecules, particles, or traces analyzed for each assay is indicated in the corresponding figure legends or in the relevant Methods sections. No data were excluded from the analyses unless explicitly stated. Statistical tests and exact p-values are reported in the figures or figure legends. Unless otherwise stated, data are presented as mean ± SEM. Confidence intervals are reported where applicable.

For SeRP experiments, enrichment values and 95% confidence intervals were calculated using the Agresti-Coull binomial method (single gene profiles) or bootstrapping (metagene profiles), implemented either in the RiboSeqTools R package (https://github.com/ilia-kats/RiboSeqTools) or in custom in-house Python scripts. Background distributions were generated by randomly sampling five positions per gene included in the analysis. Statistical significance of features associated with NAC binding to emerging nascent chains (Figures S2, S3, and S4) was assessed using two-sided Mann-Whitney U tests, with p-values reported in the corresponding figure legends. Changes in translation levels upon NAC depletion were also evaluated using two-sided Mann-Whitney U tests. Gene Ontology (GO) enrichment analyses were performed using DAVID v6.8 with custom background datasets matched to the tested protein sets. Adjusted p-values were calculated using the Benjamini-Hochberg procedure, and GO terms with adjusted $p < 0.05$ were considered significant. Enrichment of domain topology and protein architecture was assessed by calculating fold enrichment relative to background, with statistical significance determined using Fisher's exact test. Position-specific enrichment of secondary structure elements and amino acid identities was assessed using Two Sample Logo with default parameters, and significance thresholds were defined by the tool. Parameters used for single-molecule FRET analyses are described in the corresponding methods section. Cryo-EM data processing was performed using cryoSPARC, and particle numbers at each processing step are reported in the methods. Consistency between replicates was confirmed. Statistical significance of force-extension measurements was assessed using either the Mann-Whitney U test or a one-tailed two-proportion Z-test, as indicated in the corresponding figure legends.